Cell Reports
Medicine

Article

Stage-stratified molecular profiling of non-muscle-invasive bladder cancer enhances biological, clinical, and therapeutic insight

Graphical abstract

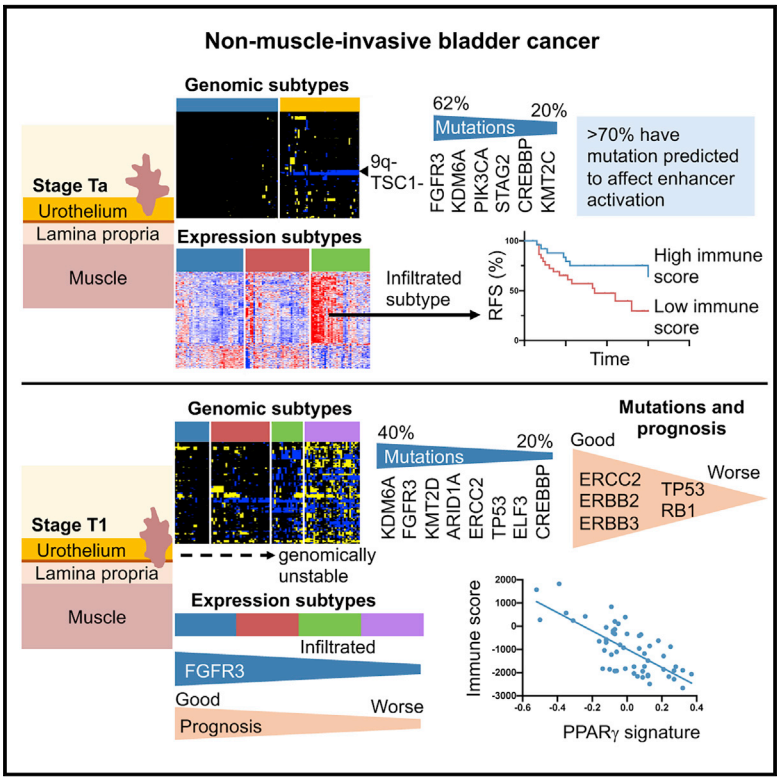

Highlights

- Separate subtyping of stage Ta (non-invasive) and T1 (submucosal invasion) tumors
- Increased biological understanding compared with subtypes derived from all NMIBCs
- Infiltrated subtypes of Ta and T1 with relationship to PPARG activity
- Differential prevalence of cisplatin sensitivity-related mutations in T1 subtypes

Authors

Carolyn D. Hurst, Guo Cheng, Fiona M. Platt, ..., Lars Dyrskjøt, Mattias Höglund, Margaret A. Knowles

Correspondence

m.a.knowles@leeds.ac.uk

In brief

Hurst et al. compare molecular subtyping of all NMIBCs with separate subclassification of stage Ta (non-invasive) and T1 (submucosal invasion) tumors. They show that overall NMIBC subtypes are no more prognostic for T1 tumors than stage alone. However, stage-stratified subclassification identifies clinically relevant features and biological insights and promises improved prognostication.

Hurst et al., 2021, Cell Reports Medicine 2, 100472
December 21, 2021
https://doi.org/10.1016/j.xcrm.2021.100472

CellPress

Cell Reports Medicine

CellPress
OPEN ACCESS

Article

Stage-stratified molecular profiling of non-muscle-invasive bladder cancer enhances biological, clinical, and therapeutic insight

Carolyn D. Hurst,[1] Guo Cheng,[1] Fiona M. Platt,[1] Mauro A.A. Castro,[2] Nour-al-dain S. Marzouka,[3] Pontus Eriksson,[3] Emma V.I. Black,[1] Olivia Alder,[1] Andrew R.J. Lawson,[4] Sia V. Lindskrog,[5,6] Julie E. Burns,[1] Sunjay Jain,[7] Jo-An Roulson,[8] Joanne C. Brown,[1] Jan Koster,[9] A. Gordon Robertson,[10] Inigo Martincorena,[4] Lars Dyrskjøt,[5,6] Mattias Höglund,[3] and Margaret A. Knowles[1,11,*]

[1]Division of Molecular Medicine, Leeds Institute of Medical Research at St James's, St James's University Hospital, Beckett Street, Leeds LS9 7TF, UK
[2]Bioinformatics and Systems Biology Laboratory, Federal University of Paraná, Curitiba, Brazil
[3]Division of Oncology, Department of Clinical Sciences, Lund University, Lund, Sweden
[4]Cancer, Ageing and Somatic Mutation Programme, Wellcome Sanger Institute, Hinxton CB10 1SA, UK
[5]Department of Molecular Medicine, Aarhus University Hospital, Aarhus, Denmark
[6]Department of Clinical Medicine, Aarhus University, Aarhus, Denmark
[7]Pyrah Department of Urology, St James's University Hospital, Beckett Street, Leeds LS9 7TF, UK
[8]Department of Histopathology, St James's University Hospital, Beckett Street, Leeds LS9 7TF, UK
[9]Laboratory for Experimental Oncology and Radiobiology, Center for Experimental and Molecular Medicine, Amsterdam University Medical Centers, University of Amsterdam, Cancer Center Amsterdam, Meibergdreef 9, 1105 AZ Amsterdam, the Netherlands
[10]Canada's Michael Smith Genome Sciences Center, BC Cancer, Vancouver, BC V5Z 4S6, Canada
[11]Lead contact
*Correspondence: m.a.knowles@leeds.ac.uk
https://doi.org/10.1016/j.xcrm.2021.100472

SUMMARY

Understanding the molecular determinants that underpin the clinical heterogeneity of non-muscle-invasive bladder cancer (NMIBC) is essential for prognostication and therapy development. Stage T1 disease in particular presents a high risk of progression and requires improved understanding. We present a detailed multi-omics study containing gene expression, copy number, and mutational profiles that show relationships to immune infiltration, disease recurrence, and progression to muscle invasion. We compare expression and genomic subtypes derived from all NMIBCs with those derived from the individual disease stages Ta and T1. We show that sufficient molecular heterogeneity exists within the separate stages to allow subclassification and that this is more clinically meaningful for stage T1 disease than that derived from all NMIBCs. This provides improved biological understanding and identifies subtypes of T1 tumors that may benefit from chemo- or immunotherapy.

INTRODUCTION

More than 70% of bladder tumors are non-muscle-invasive bladder cancers (NMIBCs), with over 380,000 diagnosed per annum worldwide.[1] Affected individuals suffer frequent recurrence, necessitating long-term cystoscopic monitoring, with associated morbidity and high cost. Overall, bladder cancer is more expensive to treat than other cancers because of the cost of managing NMIBC.[2] The majority are stage Ta tumors that do not penetrate the epithelial basement membrane, but approximately 20% are stage T1 that invade the submucosa and have a high risk of progression to muscle invasion.[3] Knowledge of the molecular landscape of these tumors is incomplete. For T1, prognostic biomarkers are needed, and for all NMIBCs, improved biological understanding should allow development of novel localized therapies to reduce or eliminate risk of recurrence and progression.

NMIBCs are molecularly and clinically heterogeneous. Expression analysis has identified subclasses with relationships to outcome[4,5] and expression signatures with prognostic value.[6-8] Analysis of all tumor grades and stages has also identified transcriptional subgroups, one of which, "urothelial-like," predominates in NMIBC.[9] Similarly, DNA copy number and mutation analyses reveal genomic diversity,[10-13] with some genomic signatures showing relationships to outcome.[14] However, detailed understanding of the relationships of genomic and expression features and of tumor phenotype is lacking, and the clinical implications of NMIBC subtypes require further clarification.

Longitudinal studies of primary NMIBC and recurrences in the same individual show sequential acquisition of molecular alterations and subclonal evolution.[15,16] Instillation of mitomycin C in Ta disease and Bacillus Calmette-Guérin (BCG)or courses of

intravesical chemotherapy in T1 disease can cause further genomic alterations, induce transcriptional changes, and impose selective pressure. Thus, for discovery of diagnostic and prognostic molecular information, analysis of primary tumors is important. To improve understanding of the biology of NMIBC and evaluate the potential of molecular subtyping to add information at the time of diagnosis, we focused on primary tumors. We provide the largest whole-exome sequence dataset for T1 tumors and, using copy number, mutation, and transcriptome profiling, explore the values of combining stage Ta and T1 samples and of separating into tumor stage groups for analysis. We show that the latter provides deeper insights into biology and clinical behavior, and suggestions for therapy.

RESULTS

Study design, samples, and analysis platforms

Fresh-frozen tissues from 113 stage Ta and 104 high-grade stage T1 bladder tumors and paired blood samples were analyzed. Apart from 10 T1 samples, all were primary tumors. Follow-up data were available for 107 individuals with Ta disease and 88 with T1 disease (median, 55 months). Recurrence was recorded in 45% of Ta and 47% of T1 cases. A single Ta case and 16 T1 cases progressed to muscle-invasive bladder cancer (MIBC) or metastatic bladder cancer. Clinicopathologic information and analysis platforms are given in Table S1A. All were analyzed for copy number alterations and genome-wide mRNA expression. Whole-exome data were obtained for 58 T1 samples, and all other samples were analyzed using targeted sequencing (Table S2).[13]

Studies by the UROMOL consortium show that analysis of NMIBC separately from MIBC provides improved biological understanding and prognostic information.[4,5] Because Ta and T1 tumors show distinct clinical behavior, we hypothesized that further information could be gained by separate analysis. Thus, we compared analysis of the entire dataset with separate analysis of Ta and T1 samples.

Combined analysis of NMIBC

Unsupervised clustering of copy number (CN) data revealed 4 clusters (CN1–CN4) of increasing genomic complexity, with Ta samples contained largely in CN1 and CN2 and T1 samples in CN3 and CN4 (Figures 1A and 1B). The fraction of genome altered (FGA) increased dramatically from CN1 to CN4 (Figure S1A). High FGA was associated with worse progression-free survival (PFS) (Figure S1B) but not recurrence-free survival (RFS). There was differential distribution of the most common mutations with most *TP53* mutations in CN4 and a predominance of *FGFR3* mutations in CN1 and CN2 (Figure 1C).

We used two-stagenon-negative matrix factorization (NMF) analysis (k = 2–5) to discover transcriptional subtypes. The two initial groups segregated samples largely according to stage. Independent analysis of these groups generated 4 subtypes (E1–E4) (Figures S1C and 1D). Alignment of transcriptional and CN subtypes showed most alignment between complex CN samples (CN4) and E3. E1 contained largely CN1 and CN2 samples (Figure 1E). *TP53* mutations were predominantly in E3, *FGFR3* and *KDM6A* in E1 and E2, and *STAG2* in E1 (Figure 1F).

Gene Ontology analysis showed upregulation of categories related to protein synthesis in the first of the two initial groups and cell cycle and immune response in the second, features that dominated when Ta were compared with T1 tumors. In pairwise analysis of E1–E4, E4 had lowest expression of a compiled urothelial differentiation signature.[9,18] An FGFR3 mutation-associated signature[9] was higher in E1 and E2 and a score for immune cells[19] in E4. Cell cycle and DNA repair signatures were also differentially distributed (Figures 1F and S2A–S2D).

RFS was unrelated to CN subtype, but expression subtypes had differential RFS that approached significance, with E3 differing significantly from E2 (Figure S2E). CN and expression subtypes showed differences in PFS (Figures 1G and H) related to expression of progression and carcinoma *in situ* (CIS) signature scores,[7,17,20] with the infiltrated subtype (E4) having a better outcome than E3 (Figures 1F, 1I, and 1J).

These subtypes were clearly associated with tumor stage (Figures 1B and 1D) but did not provide additional prognostic information. Because this is most urgently needed for T1 tumors, we asked whether subtype assignment had prognostic utility when applied to T1 tumors alone. Importantly, we found no differences in PFS between the subtypes (Figure S2F). This suggests that, although diversity within the dataset allowed robust classification, this provided little information beyond the known worse outcome of T1 disease.

The UROMOL study also identified 4 expression classes of NMIBC.[5] UROMOL2021 class assignments were derived, and these aligned with good concordance (Figure 1F). Most progression events occurred in UROMOL2021 class 2a/E3, followed by class 2b/E4. E1 and E2 aligned closely with UROMOL2021 classes 1 and 3, which also show higher expression of early cell cycle genes and FGFR3-related signature. UROMOL2021 classes 2a and 2b have higher expression of late cell cycle and DNA repair genes, as in E3 and E4 (Figures 1F and S2B–S2D). We conclude that both cohorts have similar features and that the distinct subclassification methods generated similar results. We also classified the samples according to the LundTax system.[21] E1 and E2 samples were almost all classified as UroA. All but one sample classified as genomically unstable (GU) were E3/UROMOL2021 class 2a, and UroB samples were all E4/UROMOL2021 class 2b (Figure 1F). As with the subtypes derived here, neither of these systems showed a significant relationship to PFS in stage T1 samples only (log rank analysis; p = 0.46 and 0.67, respectively).

Independent analysis of stage Ta samples

CN and mutational features

Previously, we defined two groups of Ta tumors, designated genomic subtypes 1 and 2 (GS1 and GS2), demarcated largely by loss of chromosome arm 9q in GS2. Expression data of a subset identified mTORC1 signaling as the most significant difference.[13] These subtypes are shown in Figure 2A. In this expanded transcriptional dataset, we confirmed upregulation of late cell cycle, DNA repair, cholesterol synthesis, and unfolded protein response genes in GS2, compatible with loss of the 9q mTORC1 regulator TSC1 (Figure S3A). Despite this difference, these subtypes were not related to grade or RFS, although tumor grade was related to RFS (Figure S3B).

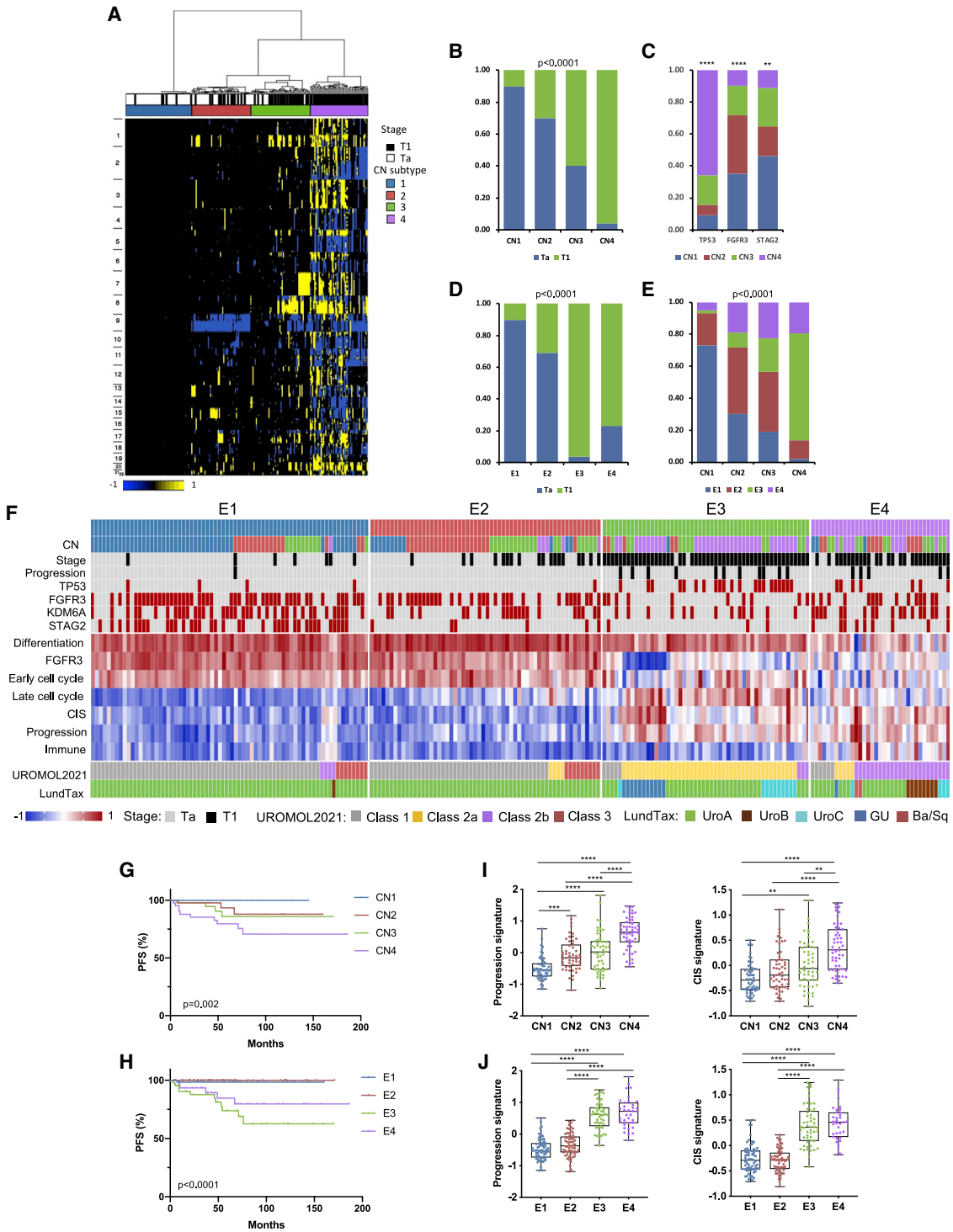

Figure 1. Combined molecular analysis of stage Ta and T1 NMIBC tumors

(A) CN clusters. Columns, samples; rows, genomic position; yellow, gain; blue, loss. Left: chromosome number. Top: cluster designation and stage.

(B) Relationship of tumor stage to CN subtype.

(C) Distribution of common mutations according to CN subtype.

(D) Relationship of tumor stage to expression subtype.

(E) Relationships of CN and expression subtypes.

(B–E) Chi square test (with Bonferroni correction in B, D, and E).

(legend continued on next page)

Mean non-synonymous mutation frequency from targeted sequencing (Table S2) was 7.9 mutations per megabase (median, 7.55) and C > T and C > G mutations dominated (43% and 25%). The single base substitution (SBS) signatures SBS2 and SBS13 (https://cancer.sanger.ac.uk/signatures/sbs/), which are attributed to activity of the APOBEC family of cytidine deaminases, accounted for 35% of single-nucleotide variants (SNVs), with 29% of tumors showing 50% or more and 61% showing 25% or more such mutations. These mutations were more common in GS2, consistent with increased expression of APOBEC3A, APOBEC3B, and APOBEC3H (Figures S3C and S3D).

As in previous studies by us and others, *FGFR3* mutations were most common (62%), followed by *KDM6A, PIK3CA*, and *STAG2*. Genes mutated in 10% or more of tumors included *KMT2A*, *KMT2C*, *KMT2D*, *CREBBP*, *EP300*, *RYR2*, *CDKN1A*, *ATM*, *ZFP36L1*, and *TSC1* (Figure 2B; Table S1B). *FGFR3* and *HRAS* mutations were mutually exclusive, with one or other in 70%. Compatible with 9q location, *TSC1* mutations were more common in GS2 ($p = 0.0016$). *KMT2D* mutations were more common in GS1 and *KMT2A* mutations in GS2 ($p = 0.038$ and 0.027, respectively).

The histone methyltransferases KMT2C, KMT2D, and KDM6A participate in large multisubunit KMT2C/D COMPASS-like complexes that are recruited to enhancers via interaction with transcription and pioneer factors. KMT2C and KMT2D carry out monomethylation of H3K4, and this, together with H3K27 acetylation by the acetyltransferases CREBBP and EP300, leads to enhancer activation.[22] One or more COMPASS-like complex components were mutated in 65% of samples, and 34% had *CREBBP* or *EP300* mutation so that 73% had a mutation predicted to affect enhancer activation (Figure 2C). Of the 7 most common mutations identified, *FGFR3* and *KMT2D* mutations were associated with higher tumor mutational burden (TMB) (Figure 2D). Although *FGFR3* mutation is linked to an APOBEC mutational process,[23] we found no relationship to APOBEC mutations or expression. Only *PIK3CA* mutation was related to RFS (Figure 2E), and no relationship of TMB and RFS was found.

Three Ta transcriptional subtypes

NMF analysis identified three expression subtypes (TaE1, TaE2, and TaE3) (Figure S3E). TaE1 and TaE3 contained many GS1 tumors and TaE2 the majority of GS2 (Figures 2A, 2F, and S3F) and high-grade tumors ($p = 0.0034$). Differences in mutation frequency of *STAG2* and *KMT2D* ($p = 0.0028$ and 0.0119, respectively) (Figure 2F) and RFS were found (Figure 2G).

We examined differential expression between subtypes (Figure S3G; Table S3). TaE1 was enriched in Gene Ontology categories associated with RNA transcription and protein synthesis (Figure S4A) and many small nucleolar RNAs (snoRNAs) that play a major role in rRNA modification (Figure S4B; Table S4). TaE2 was enriched in features of GS2, including late cell cycle genes, cholesterol homeostasis, fatty acid metabolism, response to hypoxia, and glycolysis. Features related to cell division included "sister chromatid segregation" (Gene Ontology [GO]:819), including STAG2, which had fewest mutations in TaE2 (Figures 2F and S3G). TaE2 also had highest expression of the HIF1α-regulated long non-coding RNA UCA1[24] (Figure S4C), compatible with activated mTORC1. *FGFR3* mutation was directly related to the *FGFR3*-associated signature (Figure S4D). Expression of transcriptional regulators implicated in urothelial development and differentiation was higher in TaE1 (Figure S4E).

Regulon analysis[25-27] identified 373 with significant activity. These were strongly associated with subtypes, confirming their biologically distinct features (Figure S4F). Two major patterns of activity were revealed, with TaE2 showing differences from TaE1 and TaE3 (Figure 2F), including E2F1, E2F2, and FOXM1 regulons, compatible with enhanced cell cycle activity. SREBF2 activity reflected the preponderance in TaE2 of GS2 tumors with upregulated sterol and lipid synthesis. TaE1 and TaE3 had activity of KLF5 and GRHL2, factors associated with urothelial differentiation.[28,29] Both also had higher activity of AR, TP53 and TP63 regulons, and activity of anterior HOXA genes and RXRA was enriched. TaE3 differed from TaE1 in activity of the interferon regulatory factors IRF4 and IRF8 and other factors involved in immune regulation (MSC, EOMES, IKZF1, and SPI1). This analysis also revealed some heterogeneity within the subtypes, suggesting that further subclassification is possible (Figure S4F).

Ta tumors with increased immune infiltration have the lowest recurrence rate

All comparisons with TaE3, which had improved RFS compared with other subtypes, identified "immune response" (GO:6955) (Figure S4G) and terms related to the inflammatory response (Table S3). ESTIMATE immune scores[30] and PD-L1 expression were elevated (Figure 2H). Differential RFS was found in individuals with the highest and lowest immune infiltration scores independent of subtype (Figure 2I), but immune scores were not related to mutations or FGA despite more GS1 samples in the infiltrated subtype (Figure S3F).

We interrogated the nature of the immune infiltrate.[31] Interferon signaling was highest in TaE3 ($p < 0.0001$), and significant infiltration by plasma cells ($p = 0.002$), T cells ($p < 0.0001$), macrophages ($p < 0.0001$), monocytes ($p = 0.014$), and neutrophils ($p = 0.001$) was detected. Expression profiles for activated CD8+ and effector memory CD8+ T cells, related to cancer immunogenicity,[32] and a T regulatory (Treg) cell signature[19]

(F) Top: distribution of CN subtypes, stage, common mutations, and disease progression according to expression subtype. Black, stage T1/progression; red, mutation present. Center: gene expression signatures (standardized *Z* scores) with differential expression across subtypes ($p < 0.0001$). Bottom: alignment to UROMOL2021 and LundTax classifications.

(G) Progression-free survival (PFS) stratified according to CN subtype.

(H) PFS according to expression subtype.

(G and H) Log rank analysis.

(I) 12-gene progression risk score[7] and weighted CIS score[17] in CN subtypes.

(J) 12-gene progression risk score and weighted CIS score in expression subtypes.

(I and J) Kruskal-Wallis test with Dunn's multiple comparison correction.

Mean, 25th and 75th percentiles, and minimum and maximum values are shown. ****$p < 0.0001$, ***$p < 0.001$, **$p < 0.01$. See also Figures S1 and S2.

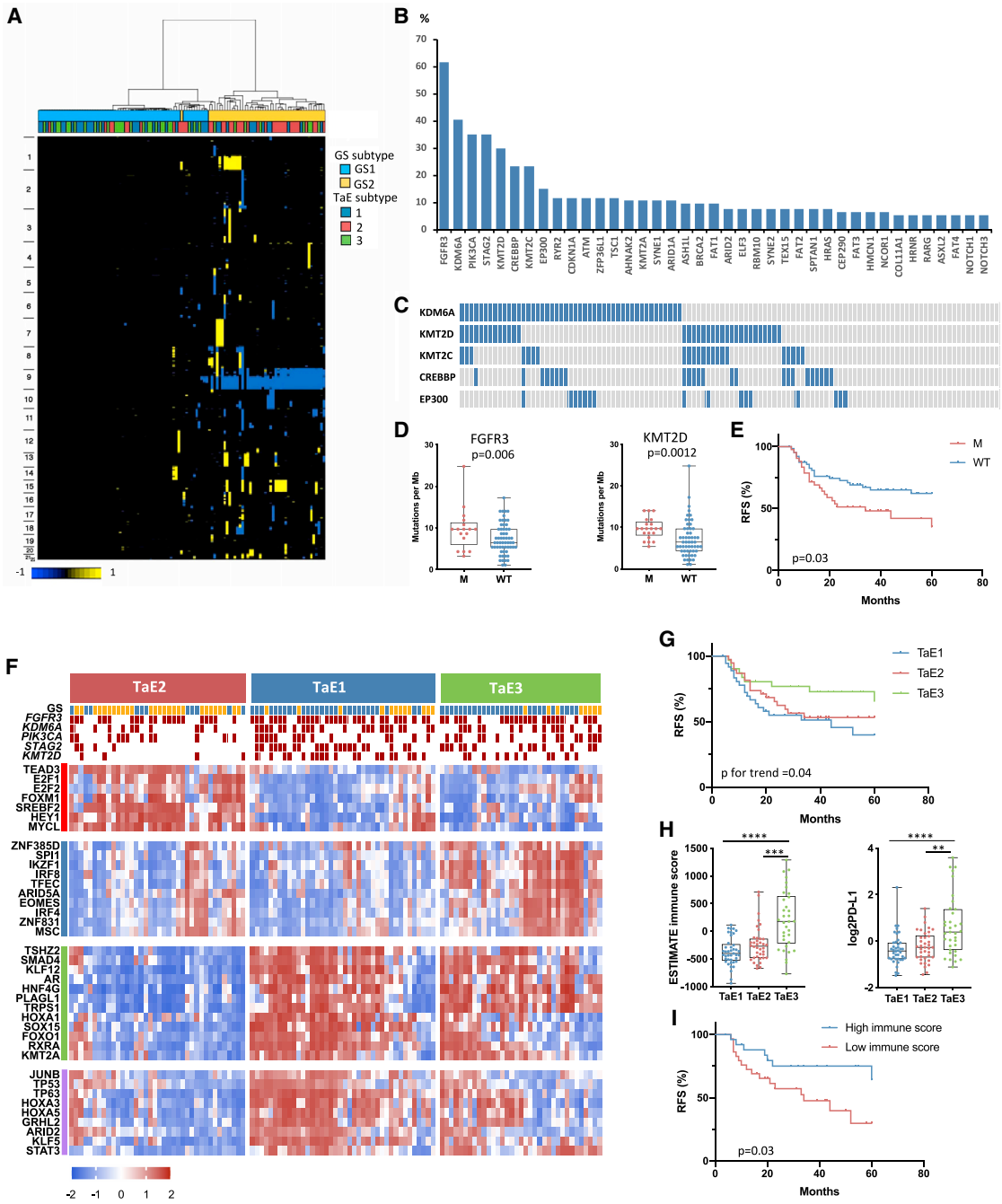

Figure 2. Independent molecular analysis of stage Ta tumors

(A) CN clusters. Columns, samples; rows, genomic position; yellow, CN gain; blue, CN loss. Left: chromosome number. Top: genomic and expression subtype.

(B) Frequencies of mutations identified by targeted sequencing.

(C) Mutations in chromatin modifier genes that affect enhancer activation status. Blue, mutant; gray, wild type.

(D) TMB as SNVs per megabase according to *FGFR3* and *KMT2D* mutation. Mann-Whitney test.

(E) Recurrence-free survival (RFS) according to *PIK3CA* mutation status. M, mutant; WT, wild type.

(F) Top: distribution of GS and selected mutations according to expression subtype. Blue, GS1; yellow, GS2; red, mutation present. Lower heatmaps show regulon activity (dES values). Blocks are color coded (left) according to regulon clusters in Figure S4F.

(G) RFS according to expression subtype.

(H) ESTIMATE immune score (left) and expression levels of CD274 (PD-L1) (right) according to expression subtype. Kruskal-Wallis test with Dunn's multiple comparison correction.

(legend continued on next page)

were elevated (Figure S4H). Despite expression of immunosuppressive biomarkers, cytolytic activity estimated from granzyme (GZMA) and perforin (PRF1) expression was also higher in TaE3 (Figure S4I). This suggests that longer RFS in TaE3 is related to an upregulated anti-tumor response.

Independent analysis of stage T1 tumors

CN and mutational features

Although stage T1 tumors share features with MIBC, their molecular landscape has not been well studied. We defined four CN subgroups (T1CN1–T1CN4). T1CN1 had few CN alterations, including chromosome 9 deletions, and T1CN3 was dominated by losses rather than gains (Figure 3A). FGA increased from T1CN1 to T1CN4 (Figure S5A). Alterations conformed to our previous findings,[10] with frequent losses of 2q (40%), 9p (52%), 9q (52%), 11p (48%), and 17p (40%) and gains of 1q (51%), 5q (27%), 8q (52%), 17q (28%), and 20q (48%). Regions of amplification were identified on 14 chromosome arms. The most common were on 3p25.1 in 7% of samples (*NUP210* and *IQSEC1*), 3p25.2 in 9% (including *PPARG* and *RAF1*), 6p22.3 in 8% (including *E2F3*, *SOX4*, and *CDKAL1*), 8q22.2-q22.3 in 6% (including *YWHAZ*, *GRHL2*, and *KLF10*), 11q13.3 in 13% (including *CCND1*, *FGF19*, *FGF4*, and *FGF3*), and 12q15 in 8% (including *MDM2*). Homozygous deletions (HD) were infrequent apart from 9p21 (*CDKN2A*; 12%) (Table S5). The subtypes had similar RFS ($p = 0.6$) but showed differential PFS and a relationship of FGA to PFS (Figures S5B and S5C). In pairwise comparisons, the major expression differences were upregulation of DNA replication, DNA repair, cell cycle, and cell division gene sets in T1CN4.

Whole-exome sequencing (mean 87× coverage, 89% of bases > 30×) identified 49,477 somatic SNVs (mean 868 and median 450 per sample). Interestingly, more SNVs were present in the chromosomally stable subtype T1CN1 (Figure 3B), and PFS analysis showed a better outcome for those with medium or high TMB (Figure S5D). C > T transitions (60%) and C > G transversions (17%) dominated. NMF analysis identified two major mutational signatures, one with features of APOBEC-induced mutation, which contributed to more than 50% of mutations in 68% of samples, and a second that contained predominantly C > T and T > C, which likely represents a mixture of common signatures reported previously in bladder cancer (Figure S5E).[33] Assessment of SBS signatures[34] revealed many dominated by the APOBEC signatures SBS2 and SBS13 (79% of samples) and others containing SBS1 and SBS5; the latter is related to *ERCC2* mutation (Figure S5F).[35,36] APOBEC3A and APOBEC3B expression was higher than in Ta tumors (Figure 3C).

dNdScv analysis[37] identified 23 genes with predicted driver function (Table S6). *FAT1*, *ATM*, *RHOB*, *KRAS*, and *RBM10* fell just below the cutoff for significance, likely because of the small sample size. *FGFR3*, *PIK3CA*, and *STAG2* mutations were less frequent than in Ta (Figure 3D; Table S1B) but mutations in many genes, including *ARID1A*, *ELF3*, *ERCC2*, and *TP53* were more frequent. However, these frequencies did not align closely with those reported in MIBC[38] (Figure S5G). Importantly, this intermediate profile was not due to Ta-like or MIBC-like profiles of individual tumors but due to intermediate profiles within tumors (Figure S5H).

Two genes not implicated previously in NMIBC, KAT8 regulatory non-specific lethal (NSL) complex subunit 1 (*KANSL1*) and G protein subunit alpha 13 (*GNA13*), were predicted drivers. GNA13 is a subunit of a heterotrimeric G-protein that mediates signaling through specific G-protein-coupled receptors (GPCRs). Four of 5 mutations detected were missense mutations in codon R200. Inactivating mutations in *KANSL1*, encoding a protein found in chromatin-modifying complexes,[39,40] were found in three samples. Mutations in genes involved in the COMPASS-like complex and/or *EP300* or *CREBBP* were frequent (65%). *FGFR3* mutations were more common in T1CN1 and T1CN2 and *TP53* mutations in T1CN3 and T1CN4 (Figure 3E). *ERCC2* mutation was most common in T1CN1 (Figure 3F). Of the 6 most commonly mutated genes, *TP53* mutation was associated with worse PFS, as expected[41] (Figure 3G), and *ERCC2* mutation with favorable PFS (see below).

In MIBC, mutations in *ERCC2* and other DNA damage response (DDR) genes predict response to cisplatin-based chemotherapy[42-45] and immune checkpoint inhibitors.[46] *ERBB2* mutations are also linked to cisplatin response.[47] Because individuals with high-risk T1 disease may be considered for such therapies,[48] we evaluated the distribution of these mutations. In exome sequence data, 53% of tumors had 1 DDR gene mutation or more, with more in T1CN1 and T1CN4 (Figure 3H), associated with higher TMB (Figure 3I). In the entire series, 50% had *ERCC2*, *RB1*, *ATM*, *BRCA2*, or *ERBB2* mutations (Figure 3J).

ERCC2 mutation was present in 24% of T1 tumors compared with 4% in Ta. Apart from one frameshift, all were missense mutations in the helical motif regions (Figure 4A). Seven of these are functionally inactivating, including N238S and T484M, found in seven and three samples, respectively,[49] and 6 new mutations are close to known detrimental mutations (Figure 4B). Compatible with high TMB in T1CN1 (Figure 3B), *ERCC2* mutant tumors showed higher TMB (median, 14.84 mutations per megabase; IQR, 10.2–25.04) than wild-type tumors (median, 7.42 mutations per megabase; IQR, 4.64–11.13) (Figure 4C), and mutation was associated with favorable PFS (Figure 4D). Of other DDR genes analyzed separately, only *ATM* mutations, most not found with *ERCC2* mutation, were associated with higher TMB ($p = 0.006$). No difference in PFS was detected for those with 1 mutation or more in *ATM*, *RB1*, or *BRCA2*.

ERBB2 and *ERBB3* mutations are reported in 12% and 10% of MIBC, respectively.[38] Here, mutations were present in 14% and 16% of stage T1 (Figures 4E and 4F; Table S7). Most *ERBB2* mutations were potentially activating mutations focused in the extracellular region. 33% had focal gain of the *ERBB2* region or all of 17q, and a single tumor had high-level amplification.

(D and H) Mean, 25th, and 75th percentiles, minimum and maximum values are shown.
(I) RFS according to high (top 25th percentile) and low (lowest 25th percentile) immune score.
(E, G, and I) Log-rank analysis.
****$p < 0.0001$, ***$p < 0.001$, **$p < 0.01$. See also Figures S3 and S4.

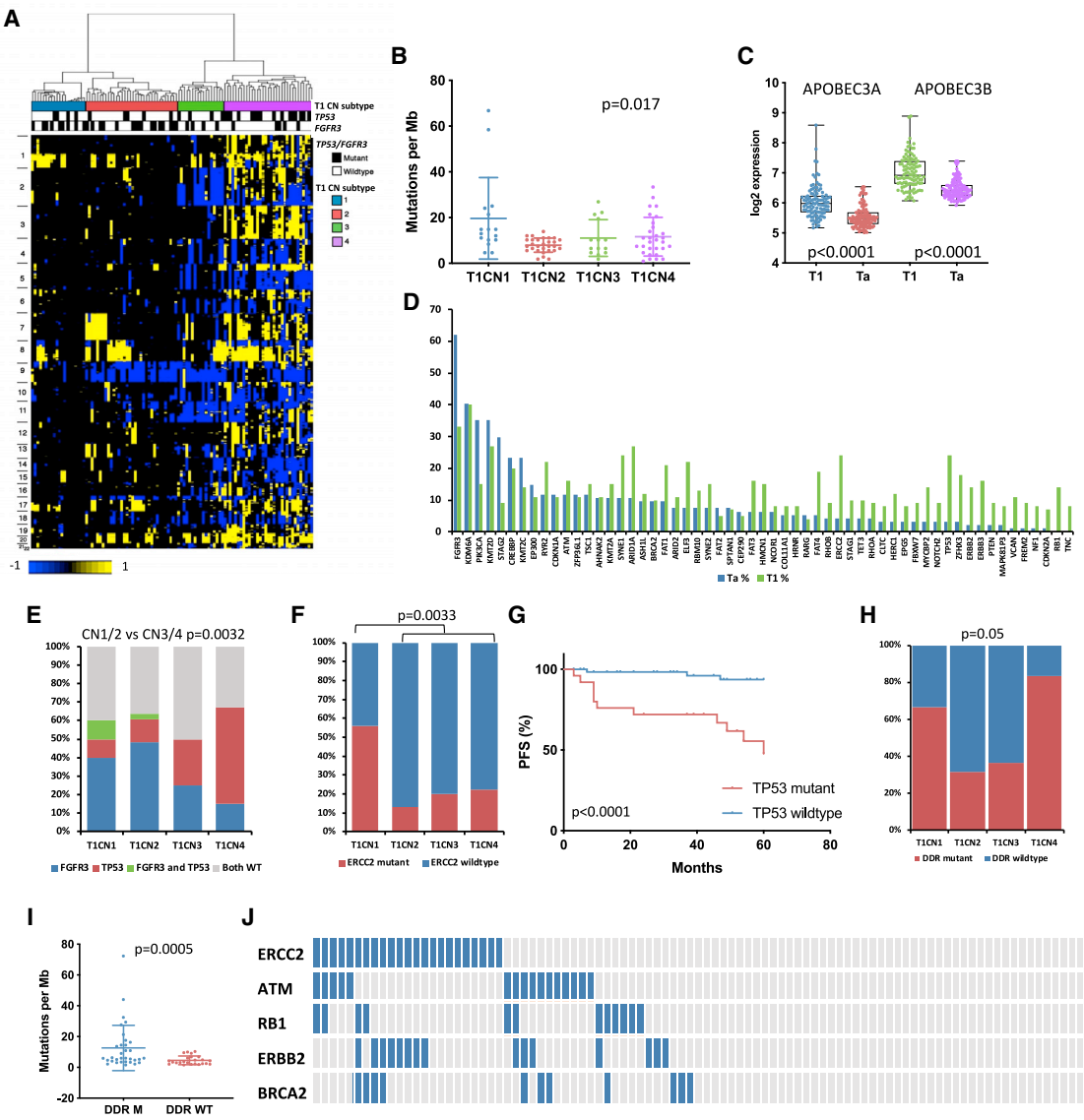

Figure 3. Independent molecular analysis of stage T1 tumors

(A) CN clusters. Columns, samples; rows, genomic position; yellow, CN gain; blue, CN loss. Left: chromosome number. Top: CN subtype and *TP53* and *FGFR3* mutation status. Black, mutation present.

(B) TMB as SNVs per megabase according to CN subtype. Kruskal-Wallis test. Bars indicate mean and SD.

(C) Expression of APOBEC3A and APOBEC3B in Ta and T1 tumors.

(D) Mutation frequencies in Ta and T1 tumors for genes mutated in 5% or more of samples in either group.

(E) Distribution of *FGFR3* and *TP53* mutations in CN subtypes.

(F) Distribution of *ERCC2* mutations in CN subtypes. Fisher's exact text.

(G) PFS according to *TP53* mutation status. Log rank analysis.

(H) Mutations in DDR genes analyzed by whole-exome sequencing (any of *ERCC2*, *ATM*, *RB1*, *ATR*, *BRCA2*, *POLE*, *FANCC*, and *CHEK2*) according to CN subtype.

(E and H) Chi-square test with Bonferroni correction.

(I) TMB as SNVs per megabase according to mutations in DDR genes (any of *ERCC2*, *ATM*, *RB1*, *ATR*, *BRCA2*, *POLE*, *FANCC*, and *CHEK2*) in tumors analyzed by whole-exome sequencing.

(C and I) Mann-Whitney test. Mean, 25th and 75th percentiles, minimum and maximum values are shown.

(J) Relationships of DDR gene mutations. Blue, mutant; gray, wild type.

See also Figure S5.

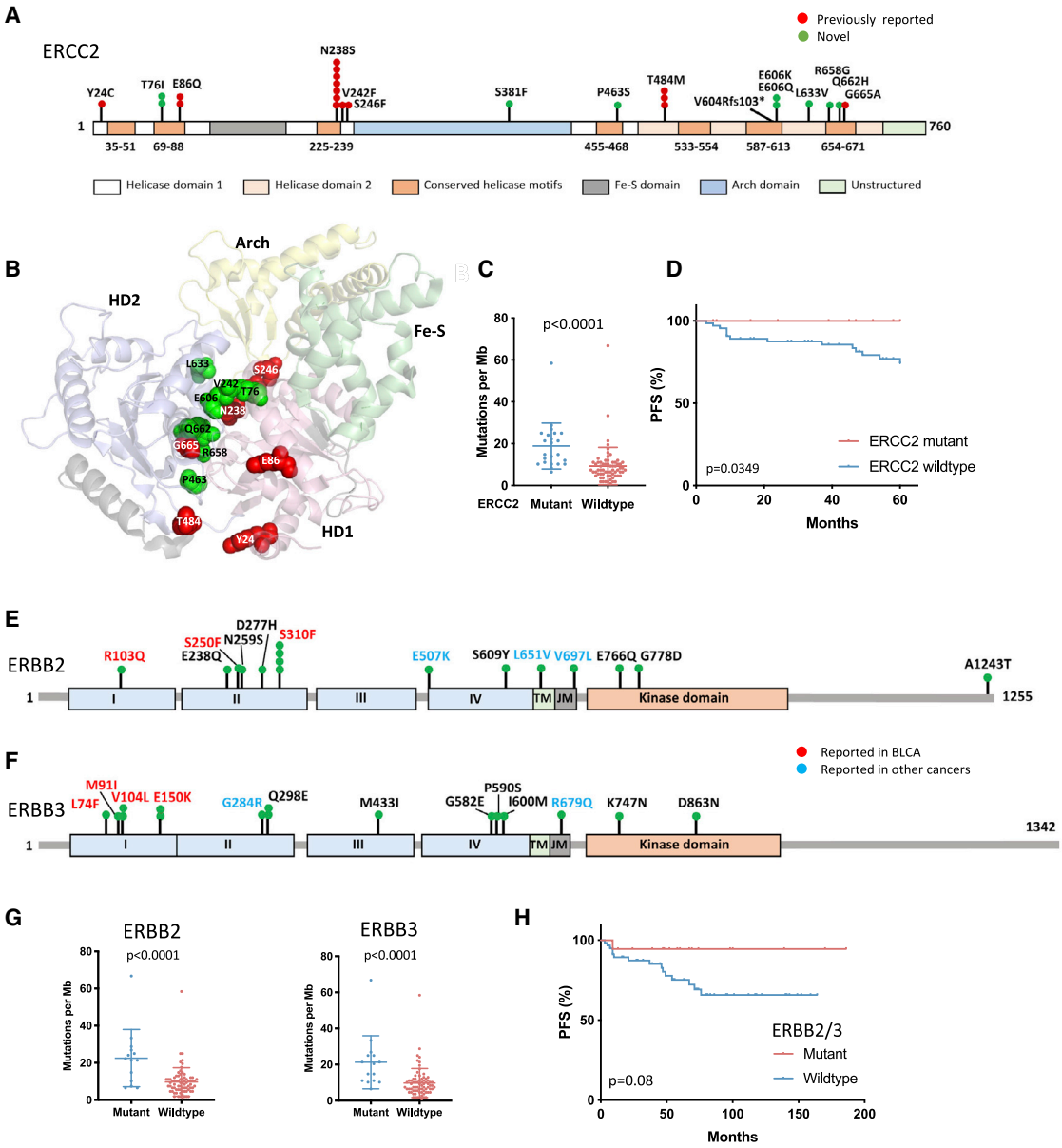

Figure 4. ERCC2, ERBB2, and ERBB3 mutations in stage T1 tumors

(A) ERCC2 protein showing positions and frequency of point mutations identified.

(B) Structure of the ERCC2 protein (PDB: 5IVW) showing positions of mutated residues. Red, residues with mutations reported previously to affect function; green, novel mutations.

(C) TMB as SNVs per megabase in *ERCC2* mutant and WT samples. Bars indicate mean and SD.

(D) PFS according to *ERCC2* mutation status.

(E) ERBB2 protein, showing positions and frequency of point mutations.

(F) ERBB3 protein, showing positions and frequency of point mutations.

(G) TMB as SNVs per megabase in *ERBB2* (left) and *ERBB3* (right) mutant and WT T1 samples. Bars indicate mean and SD.

(C and G) Mann-Whitney test.

(H) PFS according to *ERBB2* and/or *ERBB3* mutation status.

(D and H) Log rank analysis.

See also Figure S5 and Table S7.

Mutations were unrelated to CN or expression subtype, but gains were most common (60%) in T1CN4 ($p < 0.0001$). As in other tumor types,[50] 8 tumors had mutations in both receptors ($p < 0.05$). Three of only four potentially inactivating mutations in either gene were in tumors with concomitant point mutations, suggesting selection for mutant-only heterodimers. There was

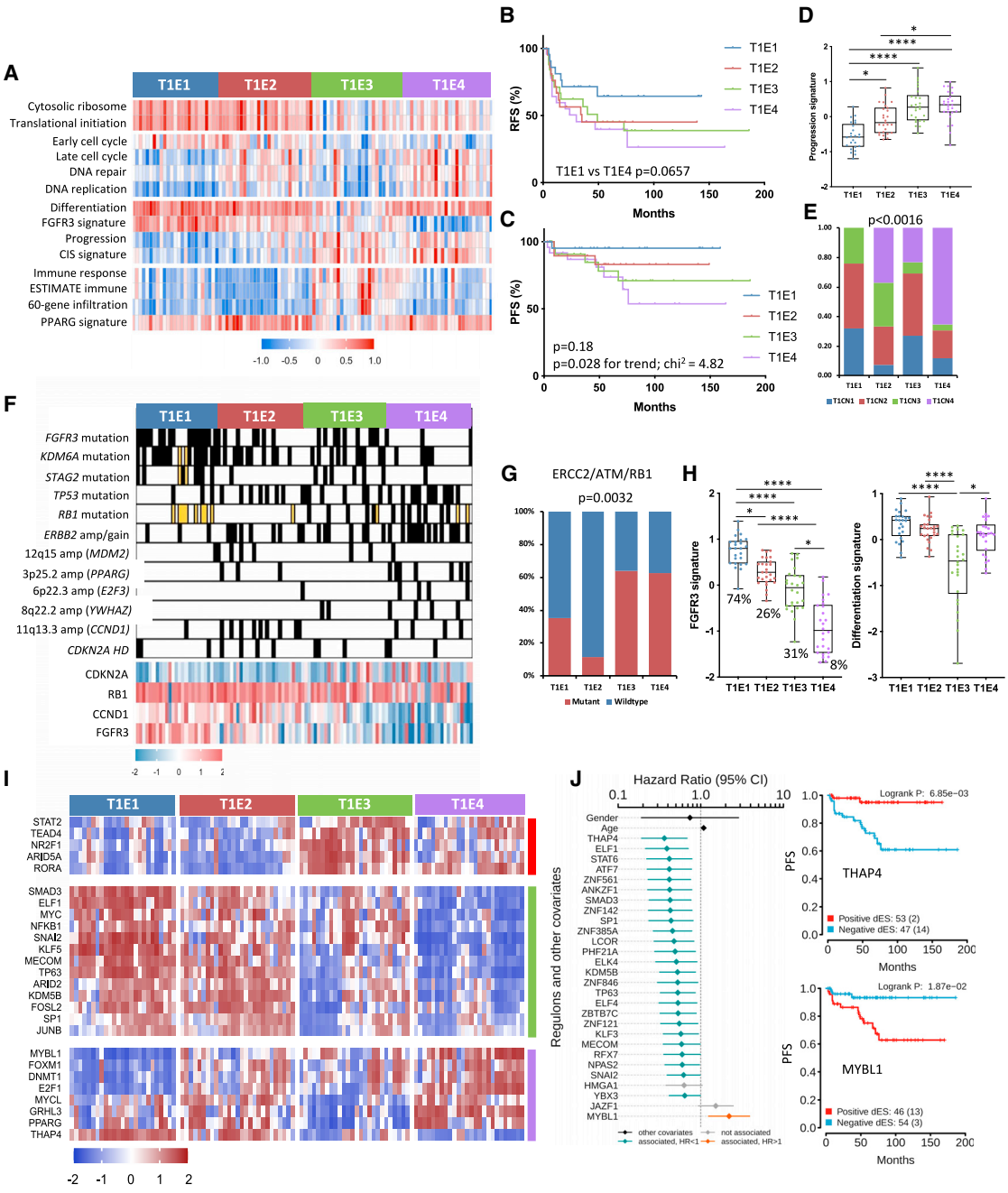

Figure 5. Features of stage T1 expression subtypes

(A) Heatmaps of *Z* scores for selected GO categories and expression signatures according to expression subtype. Cytosolic ribosome, GO:22626; Translational initiation, GO:6413; DNA replication, GO:6260; Immune response, GO:6955.

(B) RFS according to expression subtype.

(C) PFS according to expression subtype.

(D) 12-gene progression risk score in expression subtypes.

(E) Relationships of CN and expression subtypes.

(F) Selected CN alterations and gene expression according to expression subtype. Black, amplification or mutation; white, normal or WT; yellow, no data.

(G) *ERCC2*, *ATM*, and/or *RB1* mutations according to expression subtype.

(E and G) Chi-square test with Bonferroni correction.

(H) FGFR3 signature with mutation frequency and differentiation signature in expression subtypes.

(D and H) Kruskal-Wallis test with Dunn's multiple comparison correction.

(I) Regulon activity profiles according to expression subtypes. Blocks are color coded according to regulon clusters in Figure S6E.

(legend continued on next page)

co-occurrence with *ERCC2* mutation (Table S7), and, accordingly, *ERBB2* and *ERBB3* mutations were linked to high TMB (Figure 4G) and longer PFS (Figure 4H). Thus, DNA-based features can subdivide T1 tumors into subtypes with different clinical outcomes and suggest systemic chemotherapy or targeted therapies.

Four T1 transcriptional subtypes

Two-stage NMF analysis revealed four subtypes (T1E1–T1E4) (Figures 5A and S6A). Differences in RFS between T1E1 and T1E4 approached significance (Figure 5B). T1E1 showed best and T1E4 worst PFS. The progression rates at 5 years for subtypes T1E1–T1E4 were in the order 5%, 15%, 17%, and 25%, respectively. This was reflected in progression signature scores (Figures 5C and 5D). Because RFS and PFS curves showed crossing over at early time points after diagnosis (Figures 5B and 5C), we carried out Cox regression analysis to estimate the long-term survival rate under proportional and non-proportional hazard assumptions. This suggested a change in hazard ratios over time (Figure S6B). Relationships to CN subtypes and distribution of common genomic features in these subtypes are shown in Figures 5E and 5F. 6p22.3 (*E2F3*) amplification and *RB1* mutation were only found in T1E3 and T1E4, and RB1 and CDKN2A expression were inversely correlated ($r = -0.62$). *TP53* mutation was higher in T1E2, T1E3, and T1E4, which had more CN alterations (FGA in the order T1E4 > T1E2 > T1E3 > T1E1) (Figure S6C). DDR gene mutations were common in T1E3 and T1E4 (Figure 5G).

Pairwise comparison of the two initial NMF groups revealed higher expression of genes involved in translational initiation, protein targeting, and ribosome biogenesis in the first (T1E1 and T1E2) and of genes related to immune and inflammatory responses in the second (T1E3 and T1E4) (Figure 5A; Table S8). Pairwise comparisons of T1E1–T1E4 showed higher cell cycle, DNA repair, DNA replication, and metabolism-related gene expression in T1E2 and T1E4. Cholesterol and lipid biosynthesis genes and genes involved in the unfolded protein response were highest in T1E4, and categories related to glucose metabolism and canonical glycolysis highest in T1E2. T1E3 was enriched in immune and inflammatory response genes, expressed in the order T1E3 > T1E4 > T1E1 > T1E2 (Figure 5A).

The urothelial differentiation signature was high in T1E1, T1E2, and T1E4 (Figures 5A and 5H). Very low levels of this and of differentiation-associated transcriptional regulators were present in some T1E3 samples (Figure S6D). The FGFR3 signature aligned with mutation frequency (Figure 5H), correlated with early cell cycle gene expression ($r = 0.47$, $p < 0.0001$), and was inversely related to late cell cycle gene expression ($r = -0.49$, $p < 0.0001$) and CIS signature ($r = -0.78$, $p < 0.0001$).

We identified 286 regulons with differential activity (Figures 5I and S6E). E2F1 and FOXM1 activity reflects upregulated cell cycle activity in T1E4 and T1E2. As in Ta, KLF5 and TP63 activity was higher in the more differentiated subtypes. PPARG activity was reduced in T1E3, and T1E4 showed strikingly reduced levels of MYC, nuclear factor κB (NF-κB), and SMAD3 activity. Some highly active regulons in T1E3 (Figure S6E) relate to immune cell function (EOMES, MSC, AIRE, STAT4), but many do not and have no known function or are implicated in neural or testis development or function. We assessed the relationships of regulon differential enrichment scores in relation to RFS and PFS using a multivariate analysis that considered gender and age. HIF1A3 and ZBTB8B activity was associated with reduced RFS (log rank $p = 0.027$ and 0.04, respectively). Increased PFS was associated with THAP4 and ELF1 activity and reduced PFS with MYBL1 activity (Figure 5J). THAP4 and MYBL1 activities were strongly negatively correlated ($r = -0.75$, $p < 0.0001$). Examination of genes correlated with MYBL1 levels revealed negative correlation with TP63 ($r = -0.544$, $p < 0.0001$) and the PPARG coactivator PPARGC1B ($r = -0.545$, $p < 0.0001$).

A stage T1 subtype with enhanced immune infiltration

ESTIMATE stromal and immune scores were highest in T1E3 (Figure 6A). These were not related to FGA, TMB, or single mutations but had negative relationships with DNA repair gene expression[51] (ESTIMATE $r = -0.35$, $p = 0.0002$; 60-gene signature[19] $r = -0.53$, $p < 0.0001$). Deconvolution of expression data provided further insights. Hallmark gene sets for interferon γ (IFNγ) and IFNα responses were upregulated in T1E3 ($p < 0.0001$ for both). Signatures related to cytotoxic T cells, TBX21, marking Th1 helper cells, IFNG, and cytolytic response markers were present. Markers of Treg cells, interleukin-10 (IL-10) and other immunoregulatory markers (PD-L1 and CTLA4) were upregulated (Figure 6B), suggesting an active but suppressed immune response. A 6-gene T effector signature linked to favorable checkpoint inhibitor response in bladder cancer was upregulated,[52] and we noted striking upregulation of a T cell inflamed signature related to response in melanoma[53] (Figure S7A). Immune infiltration and PD-L1 expression were higher in samples from females (Figure 6C). However, immune infiltration score or T effector cell signature themselves did not predict outcome.

PPARG mutation and expression are related to immune infiltration in NMIBC

The nuclear hormone receptor PPARγ plays a key role in control of urothelial differentiation.[55] Conversely, in luminal bladder tumors, amplification, increased expression, and gain of function mutations in it and its binding partner *RXRA* are implicated in driving disease.[56,57] Upregulated *PPARG* expression and/or *RXRA* mutation is associated with evasion of immunosurveillance and reduced response to immunotherapy in MIBC.[57] Because the situation in NMIBC is not known, we assessed *PPARG* and *RXRA* mutations, *PPARG* gene amplification (3p25.2), PPARG expression, and a PPARG-related transcriptional signature.[54]

We found *PPARG* mutations in five and *RXRA* mutations in three T1 exome-sequenced tumors (14%), including a functionally active mutation (T475M)[56] and mutations near or within the ligand-binding domain of *PPARG* (Q231R, M284I, K291N,

(J) Left: Cox multivariate regression analysis showing the proportional hazards of each regulon, gender, and age, indicating the contribution of each variable to PFS. Right: Kaplan-Meier plot for PFS, stratified by positive versus negative regulon activity status for THAP4 and MYBL1. BH-adjusted p values.
(B, C, and J right) Log rank analysis.
Mean, 25th, and 75th percentiles, minimum and maximum values are shown. ****$p < 0.0001$, *$p < 0.05$. See also Figure S6.

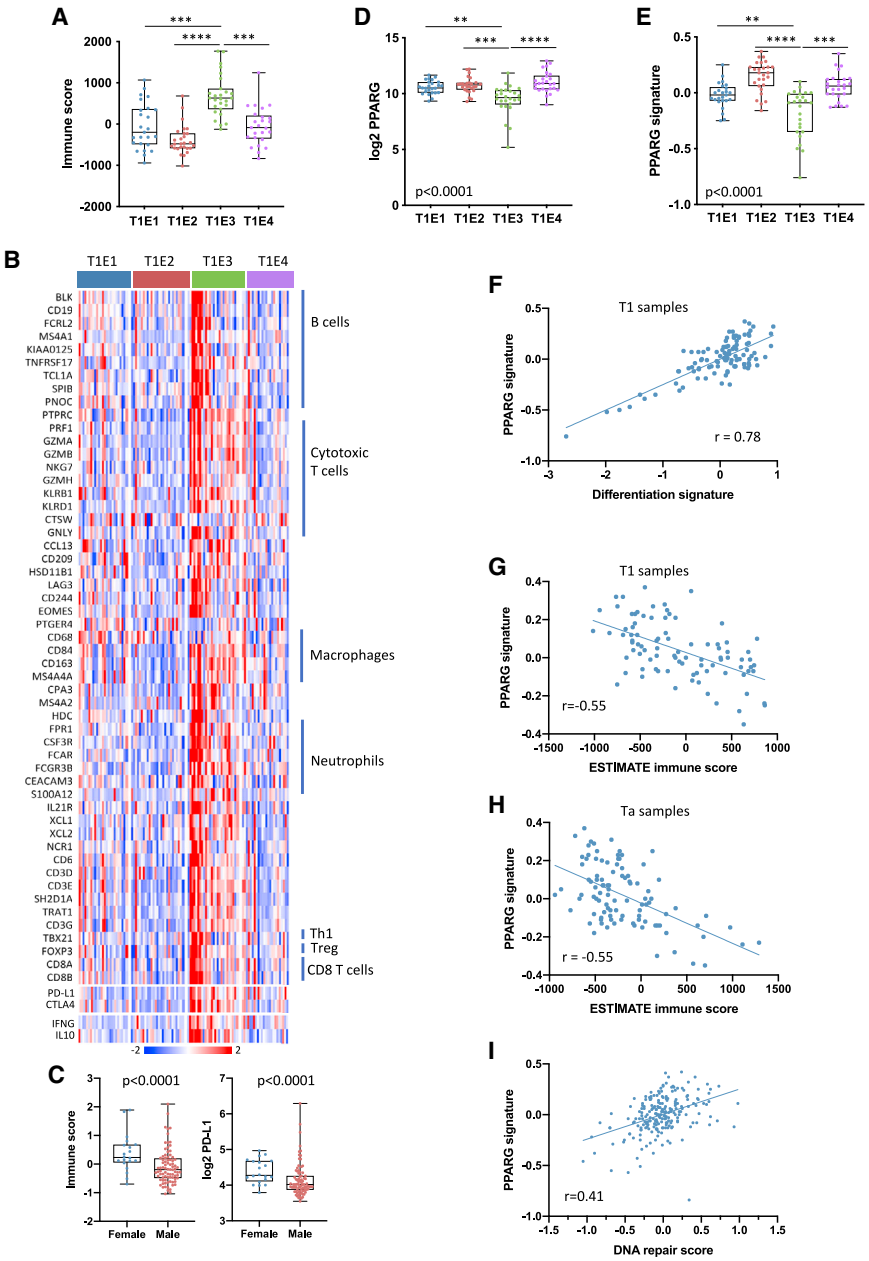

Figure 6. Immune infiltration is related to PPARG signaling in NMIBC

(A) ESTIMATE immune signature score in T1 expression subtypes.

(B) Heatmap of *Z* scores for 60-gene immune cell signature[19] in T1 expression subtypes.

(C) 60-gene immune score (left) and PD-L1 expression (right) according to gender in T1 tumors. Mann-Whitney test.

(D) PPARG expression according to T1 expression subtype.

(E) PPARG signature score[54] according to T1 expression subtype.

(A, D, and E) Kruskal-Wallis test with Dunn's multiple comparison correction. ****p < 0.0001, ***p < 0.001, **p < 0.01.

(A, C, D, and E) Mean, 25th and 75th percentiles, minimum and maximum values are shown.

(F) Correlation of PPARG signature and differentiation score in T1 tumors.

(G) Correlation of PPARG signature and ESTIMATE immune score in T1 tumors.

(H) Correlation of PPARG signature and ESTIMATE immune score in Ta tumors.

(I) Correlation of PPARG signature and DNA repair gene expression in all NMIBCs.

(F–I) Pearson r. See also Figure S7 and Table S9.

M491I). Two *RXRA* mutations (S427F) also reported in MIBC[38] are known to be activating. *PPARG* gain or amplification was present in 26%, implicating it by mutation or gain in 34% of T1 overall (Table S9). Only one *PPARG* mutation was identified in 17 Ta exome sequences analyzed and three mutations in *RXRA* in the entire Ta series (2.6%). No Ta sample had amplification.

PPARG regulon activity, PPARG expression, and the related expression signature were lowest in T1E3 (Figures 5A, 5I, 6D, and 6E). There was strong correlation of differentiation signature and PPARG signature (Figure 6F) and negative correlation of PPARG signature and immune scores (Pearson r = −0.615). We questioned whether correlation of PPARG and differentiation score was due to variations in tumor cell purity. Evaluation of two epithelial cell signatures identified 14 samples with possible lower tumor cell content (Figure S7B). With these removed, a negative relationship of ESTIMATE and PPARG scores remained (Figure 6G). Expression of chemokine chemoattractants for effector T cells that are modulated by PPARG expression in bladder tumor cells[57] was high in T1E3 (Figure S7C). Upregulated PPARG signature was associated with 6 of 8 *PPARG/RXRA* mutations. The two *PPARG*-mutant samples with no CN gain or upregulation of PPARG or its signature were in T1E3, suggesting that these mutations have no effect (Table S9).

For validation, we evaluated immune and PPARG expression signatures in two independent T1 expression datasets.[4,9] In both cases, supervised clustering identified approximately one third of samples with immune signature negatively correlated with PPARG signature (Figures S7D and S7E).

In Ta samples, the lowest PPARG signature was in TaE3, which had the highest immune infiltrate (Figure S7F). Here, correlation with differentiation signature (Figure S7G) and negative correlation with immune and PPARG scores (Figure 6H) were also found.

Finally, we examined other features suggested to relate to immune infiltration and the PPARG signature. In all NMIBCs, there was weak correlation with FGA (r = 0.17, p = 0.01) but a strong

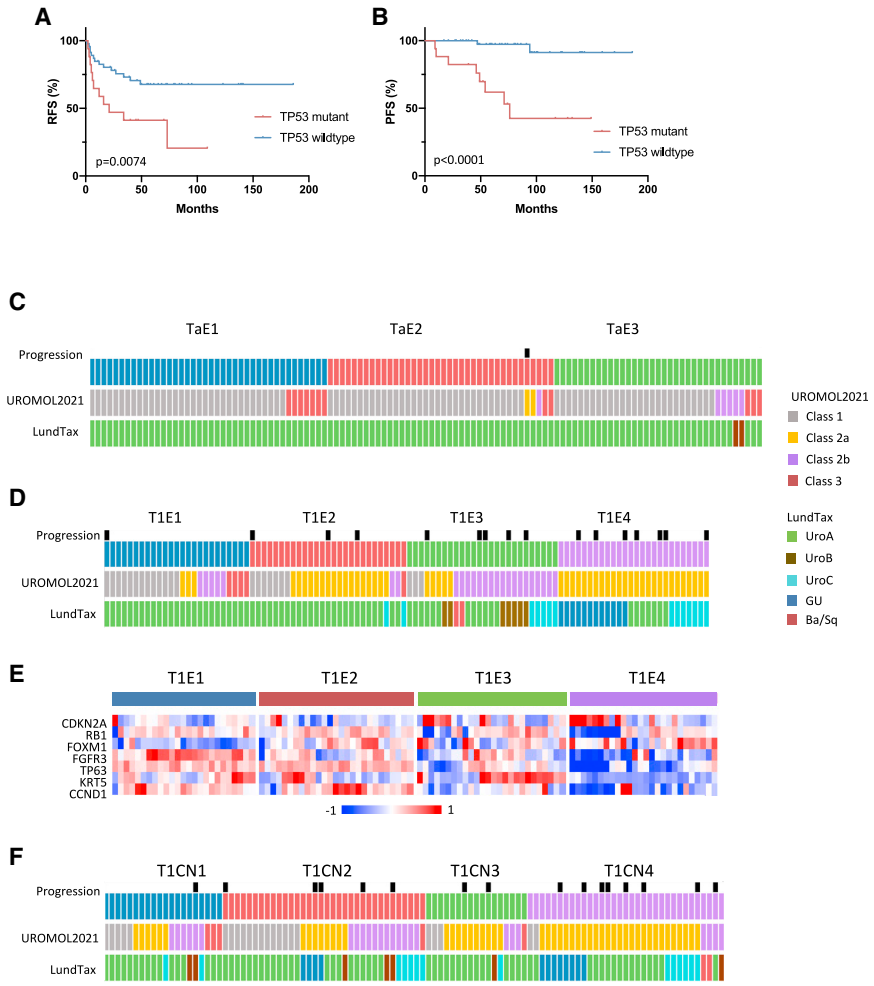

Figure 7. *TP53* mutation and outcome in BCG-treated T1 individuals and alignment of expression subtypes to UROMOL2021 and LundTax classifications

(A) RFS in BCG-treated individuals according to *TP53* mutation status.

(B) PFS in BCG-treated individuals according to *TP53* mutation status.

(A and B) Log-rank analysis.

(C) Alignment of Ta expression subtypes with UROMOL2021 and LundTax classifications.

(D) Alignment of T1 expression subtypes with UROMOL2021 and LundTax classifications.

(E) Heatmap of *Z* scores for expression of genes associated with LundTax GU subtype in T1 expression subtypes.

(F) Alignment of T1 CN subtypes with UROMOL2021 and LundTax classifications.

relationship with DNA repair gene expression[51] ($r = 0.41$, $p < 0.0001$) (Figure 6I). This was reflected in association of "DNA repair" (GO:6281) with genes positively associated with PPARG expression ($p = 4 \times 10^{-6}$). Overall, this indicates that, as in MIBC, the strength of PPARG signaling is directly related to immune infiltration and suggests a relationship of PPARG signaling to DNA repair processes.

BCG response

Sixty-three T1 individuals received a full BCG induction course and maintenance. Thirty-eight (60%) suffered no recurrence, and 10 progressed. Most progression cases were in T1E3 and T1E4 (8 of 10), but expression and CN subtype were not related to recurrence. CIS and progression signatures were related to progression ($p = 0.015$ and 0.03, respectively). No relationships with PPARG signature, ESTIMATE scores, or mutations in DDR genes were found, but only one of the 10 individuals who progressed (at 71 months) had *ERCC2* mutation compared with 25% each in the recurrence and no recurrence groups. Median TMB was 10.2 per megabase, 10.2 per megabase, and 5.6 per megabase in those with no recurrence, recurrence, or progression, respectively, but did not reach significance. Transcriptome comparison identified no differential expression between those with and without recurrence. However, there was a relationship of *TP53* mutation to post-BCG recurrence ($p = 0.02$) that was reflected in RFS ($p = 0.0074$) and PFS ($p = 0.0031$) (Figures 7A and 7B).

Alignment with UROMOL2021 and LundTax classifications

Comparison of stage-specific subtypes with UROMOL2021 and LundTax classifications (Figures 7C, 7D, and 7F) showed virtually all Ta samples classified as Lund "UroA" and many as UROMOL2021 class 1. Many T1E1 cases were UROMOL2021 classes 1, 2b, and 3. All T1E4 and many T1E2 tumors were UROMOL2021 class 2a, compatible with high late-cell-cycle gene expression in these groups (Figure 5A). UROMOL2021 class 2b aligned with T1E3, reflecting higher infiltration. There was strong alignment of T1E1, T1E2, and T1E3 with the Lund Uro subtypes, and only T1E4 samples were classified as GU ($p < 0.0001$). GU tumors have low FGFR3, CCND1, TP63, and KRT5 expression and common loss of RB1 with commensurate CDKN2A upregulation,[21] features of T1E4 (Figure 7E). Lund UroB-classified samples were all T1E3. UroB samples have a lower differentiation signature and features of squamous differentiation, including expression of KRT5 and KRT14,[58] consistent with the lowest differentiation signature (Figure 5H), and frequent KRT5 upregulation, and both samples were classified as Ba/Sq in T1E3 (Figure 7D). Alignment of CN subtypes was less clear, but UROMOL2021 class 2a aligned most closely with T1CN3 and T1CN4 (Figure 7F).

DISCUSSION

We show that, when analyzed together, NMIBCs segregate into CN and expression subtypes that align closely with tumor stage and outcome. The transcriptional subtypes were similar to those

of the UROMOL consortium.[5] In both studies, T1 tumors were predominantly in two subgroups where most progression events occurred, and in each case, the subgroup with the highest immune infiltration had fewer events. Here, these high-risk subtypes also contained LundTax subtypes GU, Ba/Sq, UroB, and UroC, all of which show a worse outcome than UroA when assessed in the TCGA MIBC dataset.[21]

Although diversity allowed robust classification that was prognostic for the entire NMIBC population, this was not useful in stage T1 subgroup analysis. Importantly, we show that stage-specific subgroups contain sufficient diversity to allow subclassification and that this provides more granular information regarding tumor biology and suggestions for therapy. It also provided prognostic information, although validation in a larger cohort is needed to determine optimal classification.

Our whole-exome analysis of paired T1 samples is the largest to date and provides an improved view of these lesions. Previous studies report that T1 tumors have a mutation spectrum intermediate between Ta tumors and MIBC. We show that this does not indicate the presence of T1 samples with an MIBC-like profile but, rather, that some T1 tumors contain Ta-like and MIBC-like mutations. It is expected that these have distinct phenotypes and that single-individual profiles will be needed for optimal management.

APOBEC enzyme expression and the related mutational profile increased from lowest levels in GS1 Ta tumors to the most genomically altered T1 tumors. In T1, SBS5, which is associated with smoking in bladder cancer,[33] and *ERCC2* mutation[35] was also identified. A relationship of FGA to T1 PFS was strongly related to *TP53* and *RB1* mutation, identifying high-risk individuals. In contrast, *ERCC2* mutant T1CN1 tumors were dominated by point mutations rather than CN events and had favorable outcomes. In addition to known associations with DDR gene mutations,[12,59,60] *ERBB2* and *ERBB3* mutations were associated with high TMB and longer PFS and might suggest bladder preservation in T1 disease.

Two predicted drivers not implicated previously in NMIBC, *GNA13* and *KANSL1*, should be included in future mutation analyses. Mutations of *KANSL1*, which is implicated as a chromatin modifier,[39,40] have been reported in 6% of MIBCs.[38] GNA13 is part of a heterotrimeric G-protein complex through which ligand-activated GPCRs signal and has several described activities.[61-64] We identified missense mutations in codon R200, close to the nucleotide binding pocket, two of which (R200G and R200K) are known to cause hyperactivation.[65] Twelve of 13 R200 mutations reported to date are in urothelial tumors (COSMIC; accessed January 18, 2021), and codon 200 mutations were found in the urothelium of three of 15 normal individuals.[66] Thus, GNA13 may be a key driver and a therapeutic target in a subset of T1 tumors.

The Ta and T1 expression subtypes showed overlap with genomic subtypes. Although the genomic drivers of T1 expression subtypes are unclear, expression features in Ta are strongly influenced by *TSC1* (9q) loss and upregulation of mTORC1 activity. In both stages we identified infiltrated subtypes. In Ta but not T1, immune score *per se* segregated individuals with differential outcomes. In T1, T1E3 and T1E4 were more infiltrated than T1E1 and T1E2, but T1E3, the more highly infiltrated of these subtypes, had improved PFS compared with T1E4. Previously suggested influences on immune infiltration showed no relationships, but our data suggest the importance of DDR gene mutation and downregulation of DNA repair genes. We also implicate PPARG signaling in driving immune evasion and, compatible with reports that PPARG influences DNA repair,[67,68] show a relationship of PPARG signaling to DNA repair gene expression. Mutations in *PPARG* and *RXRA* are as frequent in T1 as in MIBC,[56,57] and gain or amplification of *PPARG* is common. Modulation of this signaling axis may have therapeutic value alone or in combination with immune checkpoint inhibition.

Regulon analysis confirmed the distinct biology of the expression subtypes and uncovered regulators predicted to determine phenotype. This identified many regulators with still unknown functions, providing a rich resource for future analyses. Importantly, association of MYB proto-oncogene-like 1 (MYBL1) regulon activity with adverse stage T1 outcome and its negative relationship with β-barrel heme protein THAP4 activity, which may play a role in the antioxidant system,[69] may identify progression mechanisms.

Therapeutic opportunities for low-risk Ta tumors are limited to intravesical approaches, and targeting FGFR3 and the metabolic vulnerability of GS2 tumors identified here and previously[13] are rational opportunities. For individuals with stage T1 disease, immune checkpoint inhibition may be most relevant in infiltrated T1 cases that have signatures associated with a favorable response.[52,53,70] Because our data suggest that T1 tumors in females are more infiltrated, retrospective analysis in relation to gender and response in current trials in high-risk NMIBC will be of great interest.

ERCC2 and *ERBB2* mutations that are related to chemotherapy response were associated with high TMB and a good outcome. It is unclear whether co-occurrence with *ERCC2* mutation reflects an ERCC2-related mutational mechanism or whether there is a functional relationship. ERBB2 and ERBB3 could themselves be suitable targets. Notably, bladder cell lines with two of the mutations found here (ERBB2, S310F; ERBB3, V104L) are sensitive to afatinib,[71] and encouraging results have been reported for afatinib in MIBC.[72] However, systemic therapy may not be suitable for such cases if association with good outcome is confirmed.

BCG remains the mainstay of treatment for high-risk NMIBC. Because 30%–40% of individuals suffer recurrence, and approximately 10% progress,[73,74] predicting response is important. Relationships of response to high TMB,[60,75] *ERCC2* mutation,[60] higher PD-L1 expression,[76] and UroVysion fluorescence *in situ* hybridization (FISH) scores[77] have been reported. Here, most post-BCG progression occurred in T1E3 and T1E4. We found a higher but not statistically significant TMB and *ERCC2* mutation rate in individuals with a good outcome, no relationship to PD-L1 expression, and no differences in global expression between responders and non-responders. However, *TP53* mutation had a striking relationship with outcome, in accordance with some but not all previous studies.[12,59,60] The reason for these differences is unclear but indicates the need for more extensive examination of pre-BCG treatment tumor molecular status in relation to outcome and a possible need to consider germline features.

Our data indicate the feasibility of stage-specific classification. We have not generated separate classifiers for Ta and T1 tumors because moderate sample numbers may be suboptimal for generation of single sample classifiers. Because there is the possibility that submucosal invasion might be missed at the time of diagnosis, we envisage that stage Ta and T1 classifiers could be applied to all NMIBCs, and, ideally, because genomic and expression features convey prognostic information, these should be integrated to generate optimum classification.

Limitations of the study

The study is limited by relatively small numbers of samples in each separate stage group. This has not allowed development of single-sample classifiers for these groups or validation of subtype signatures in other datasets. Expanded cohorts of Ta and T1 tumors will be required to confirm the findings and to develop such classifiers. The finding of small numbers of novel mutations in T1 samples (*GNA13* and *KANSL1*) also requires confirmation in a larger cohort. As for T1 tumors, high-grade Ta tumors have a higher risk of progression. Here the majority of Ta samples analyzed were low grade, and only one individual progressed to invasive disease. Thus, it was not possible to identify features associated with high-grade Ta and/or risk of progression.

STAR★METHODS

Detailed methods are provided in the online version of this paper and include the following:

- KEY RESOURCES TABLE
- RESOURCE AVAILABILITY
  - Lead contact
  - Materials Availability
  - Data and code availability
- EXPERIMENTAL MODEL AND SUBJECT DETAILS
  - Human Tissue Samples and Subject Follow-up Data
- METHOD DETAILS
  - DNA Extraction
  - Copy Number Analysis
  - RNA Extraction, Gene Expression Profiling and NMF analysis
  - Whole Exome Sequencing
  - Targeted Sequencing
  - Tumor mutational burden
  - Mutation Significance Analysis
  - Analysis of Mutational Signatures
  - Gene expression signatures
  - Classification of samples using UROMOL2021 and LundTax classifiers
  - Regulon analysis
- QUANTIFICATION AND STATISTICAL ANALYSIS
  - Gene Ontology, KEGG Pathway and Gene Set Enrichment Analysis

SUPPLEMENTAL INFORMATION

Supplemental information can be found online at https://doi.org/10.1016/j.xcrm.2021.100472.

ACKNOWLEDGMENTS

We thank Dmitry Gordenin for helpful discussions of mutational signatures and Matthieu Rederstorff for advice on snoRNA expression. We are indebted to all individuals who gave consent for their samples to be used. This work was funded by Yorkshire Cancer Research (L376PA) and Cancer Research UK (C57387/A21777).

AUTHOR CONTRIBUTIONS

Conceptualization, C.D.H. and M.A.K.; methodology, C.D.H., G.C., F.M.P., M.A.A.C., N.-a.-d.S.M., P.E., A.R.J.L., S.V.L., J.K., A.G.R., I.M., and M.A.K.; software, M.A.A.C., N.-a.-d.S.M., P.E., A.R.J.L., S.V.L., A.G.R., and I.M.; formal analysis, C.D.H., G.C., F.M.P., M.A.A.C., N.-a.-d.S.M., P.E., O.A., A.R.J.L., S.V.L., and M.A.K.; investigation, C.D.H., G.C., F.M.P., E.V.I.B., O.A., and J.E.B.; resources, S.J., J.-A.R., J.C.B., J.K., I.M., L.D., and M.H.; data curation, C.D.H., G.C., F.M.P., and J.C.B.; writing – original draft, C.D.H., G.C., M.A.A.C., N.-a.-d.S.M., S.V.L., and M.A.K.; writing – review & editing, all authors; supervision, M.A.K.; project administration, M.A.K.; funding acquisition, M.A.K., S.J., and J.-A.R.

DECLARATION OF INTERESTS

M.A.K. has an advisory/consulting role at Janssen, LOXO Oncology, QED, and Rainier Therapeutics. L.D. has sponsored research agreements with C2i-genomics, Natera, AstraZeneca, and Ferring and an advisory/consulting role at Ferring. L.D. has received a speaker honorarium from Roche.

Received: February 9, 2021
Revised: August 9, 2021
Accepted: November 18, 2021
Published: December 21, 2021

REFERENCES

1. Ferlay, J., Colombet, M., Soerjomataram, I., Mathers, C., Parkin, D.M., Piñeros, M., Znaor, A., and Bray, F. (2019). Estimating the global cancer incidence and mortality in 2018: GLOBOCAN sources and methods. Int. J. Cancer *144*, 1941–1953.
2. Svatek, R.S., Hollenbeck, B.K., Holmäng, S., Lee, R., Kim, S.P., Stenzl, A., and Lotan, Y. (2014). The economics of bladder cancer: costs and considerations of caring for this disease. Eur. Urol. *66*, 253–262.
3. Jordan, B., and Meeks, J.J. (2019). T1 bladder cancer: current considerations for diagnosis and management. Nat. Rev. Urol. *16*, 23–34.
4. Hedegaard, J., Lamy, P., Nordentoft, I., Algaba, F., Høyer, S., Ulhøi, B.P., Vang, S., Reinert, T., Hermann, G.G., Mogensen, K., et al. (2016). Comprehensive Transcriptional Analysis of Early-Stage Urothelial Carcinoma. Cancer Cell *30*, 27–42.
5. Lindskrog, S.V., Prip, F., Lamy, P., Taber, A., Groeneveld, C.S., Birkenkamp-Demtröder, K., Jensen, J.B., Strandgaard, T., Nordentoft, I., Christensen, E., et al. (2021). An integrated multi-omics analysis identifies prognostic molecular subtypes of non-muscle-invasive bladder cancer. Nat. Commun. *12*, 2301.
6. Wang, R., Morris, D.S., Tomlins, S.A., Lonigro, R.J., Tsodikov, A., Mehra, R., Giordano, T.J., Kunju, L.P., Lee, C.T., Weizer, A.Z., and Chinnaiyan, A.M. (2009). Development of a multiplex quantitative PCR signature to predict progression in non-muscle-invasive bladder cancer. Cancer Res. *69*, 3810–3818.
7. Dyrskjøt, L., Reinert, T., Algaba, F., Christensen, E., Nieboer, D., Hermann, G.G., Mogensen, K., Beukers, W., Marquez, M., Segersten, U., et al. (2017). Prognostic Impact of a 12-gene Progression Score in Non-muscle-invasive Bladder Cancer: A Prospective Multicentre Validation Study. Eur. Urol. *72*, 461–469.
8. Patschan, O., Sjödahl, G., Chebil, G., Lövgren, K., Lauss, M., Gudjonsson, S., Kollberg, P., Eriksson, P., Aine, M., Månsson, W., et al. (2015).

A Molecular Pathologic Framework for Risk Stratification of Stage T1 Urothelial Carcinoma. Eur. Urol. *68*, 824–832, discussion 835–836.

9. Sjödahl, G., Lauss, M., Lövgren, K., Chebil, G., Gudjonsson, S., Veerla, S., Patschan, O., Aine, M., Fernö, M., Ringnér, M., et al. (2012). A molecular taxonomy for urothelial carcinoma. Clin. Cancer Res. *18*, 3377–3386.
10. Hurst, C.D., Platt, F.M., Taylor, C.F., and Knowles, M.A. (2012). Novel tumor subgroups of urothelial carcinoma of the bladder defined by integrated genomic analysis. Clin. Cancer Res. *18*, 5865–5877.
11. Nordentoft, I., Lamy, P., Birkenkamp-Demtröder, K., Shumansky, K., Vang, S., Hornshøj, H., Juul, M., Villesen, P., Hedegaard, J., Roth, A., et al. (2014). Mutational context and diverse clonal development in early and late bladder cancer. Cell Rep. *7*, 1649–1663.
12. Pietzak, E.J., Bagrodia, A., Cha, E.K., Drill, E.N., Iyer, G., Isharwal, S., Ostrovnaya, I., Baez, P., Li, Q., Berger, M.F., et al. (2017). Next-generation Sequencing of Nonmuscle Invasive Bladder Cancer Reveals Potential Biomarkers and Rational Therapeutic Targets. Eur. Urol. *72*, 952–959.
13. Hurst, C.D., Alder, O., Platt, F.M., Droop, A., Stead, L.F., Burns, J.E., Burghel, G.J., Jain, S., Klimczak, L.J., Lindsay, H., et al. (2017). Genomic Subtypes of Non-invasive Bladder Cancer with Distinct Metabolic Profile and Female Gender Bias in KDM6A Mutation Frequency. Cancer Cell *32*, 701–715.e7.
14. van Kessel, K.E.M., van der Keur, K.A., Dyrskjøt, L., Algaba, F., Welvaart, N.Y.C., Beukers, W., Segersten, U., Keck, B., Maurer, T., Simic, T., et al. (2018). Molecular Markers Increase Precision of the European Association of Urology Non-Muscle-Invasive Bladder Cancer Progression Risk Groups. Clin. Cancer Res. *24*, 1586–1593.
15. Lamy, P., Nordentoft, I., Birkenkamp-Demtröder, K., Thomsen, M.B., Villesen, P., Vang, S., Hedegaard, J., Borre, M., Jensen, J.B., Høyer, S., et al. (2016). Paired exome analysis reveals clonal evolution and potential therapeutic targets in urothelial carcinoma. Cancer Res. *76*, 5894–5906.
16. van Tilborg, A.A., de Vries, A., de Bont, M., Groenfeld, L.E., van der Kwast, T.H., and Zwarthoff, E.C. (2000). Molecular evolution of multiple recurrent cancers of the bladder. Hum. Mol. Genet. *9*, 2973–2980.
17. Dyrskjøt, L., Kruhøffer, M., Thykjaer, T., Marcussen, N., Jensen, J.L., Møller, K., and Ørntoft, T.F. (2004). Gene expression in the urinary bladder: a common carcinoma in situ gene expression signature exists disregarding histopathological classification. Cancer Res. *64*, 4040–4048.
18. Eriksson, P., Aine, M., Veerla, S., Liedberg, F., Sjödahl, G., and Höglund, M. (2015). Molecular subtypes of urothelial carcinoma are defined by specific gene regulatory systems. BMC Med. Genomics *8*, 25.
19. Danaher, P., Warren, S., Dennis, L., D'Amico, L., White, A., Disis, M.L., Geller, M.A., Odunsi, K., Beechem, J., and Fling, S.P. (2017). Gene expression markers of Tumor Infiltrating Leukocytes. J. Immunother. Cancer *5*, 18.
20. Dyrskjøt, L., Zieger, K., Kruhøffer, M., Thykjaer, T., Jensen, J.L., Primdahl, H., Aziz, N., Marcussen, N., Møller, K., and Orntoft, T.F. (2005). A molecular signature in superficial bladder carcinoma predicts clinical outcome. Clin. Cancer Res. *11*, 4029–4036.
21. Marzouka, N.A., Eriksson, P., Rovira, C., Liedberg, F., Sjödahl, G., and Höglund, M. (2018). A validation and extended description of the Lund taxonomy for urothelial carcinoma using the TCGA cohort. Sci. Rep. *8*, 3737.
22. Fagan, R.J., and Dingwall, A.K. (2019). COMPASS Ascending: Emerging clues regarding the roles of MLL3/KMT2C and MLL2/KMT2D proteins in cancer. Cancer Lett. *458*, 56–65.
23. Shi, M.J., Meng, X.Y., Lamy, P., Banday, A.R., Yang, J., Moreno-Vega, A., Chen, C.L., Dyrskjøt, L., Bernard-Pierrot, I., Prokunina-Olsson, L., and Radvanyi, F. (2019). APOBEC-mediated Mutagenesis as a Likely Cause of FGFR3 S249C Mutation Over-representation in Bladder Cancer. Eur. Urol. *76*, 9–13.
24. Xue, M., Li, X., Li, Z., and Chen, W. (2014). Urothelial carcinoma associated 1 is a hypoxia-inducible factor-1α-targeted long noncoding RNA that enhances hypoxic bladder cancer cell proliferation, migration, and invasion. Tumour Biol. *35*, 6901–6912.
25. Castro, M.A., de Santiago, I., Campbell, T.M., Vaughn, C., Hickey, T.E., Ross, E., Tilley, W.D., Markowetz, F., Ponder, B.A., and Meyer, K.B. (2016). Regulators of genetic risk of breast cancer identified by integrative network analysis. Nat. Genet. *48*, 12–21.
26. Chagas, V.S., Groeneveld, C.S., Oliveira, K.G., Trefflich, S., de Almeida, R.C., Ponder, B.A.J., Meyer, K.B., Jones, S.J.M., Robertson, A.G., and Castro, M.A.A. (2019). RTNduals: an R/Bioconductor package for analysis of co-regulation and inference of dual regulons. Bioinformatics *35*, 5357–5358.
27. Groeneveld, C.S., Chagas, V.S., Jones, S.J.M., Robertson, A.G., Ponder, B.A.J., Meyer, K.B., and Castro, M.A.A. (2019). RTNsurvival: an R/Bioconductor package for regulatory network survival analysis. Bioinformatics *35*, 4488–4489.
28. Bell, S.M., Zhang, L., Mendell, A., Xu, Y., Haitchi, H.M., Lessard, J.L., and Whitsett, J.A. (2011). Kruppel-like factor 5 is required for formation and differentiation of the bladder urothelium. Dev. Biol. *358*, 79–90.
29. Fishwick, C., Higgins, J., Percival-Alwyn, L., Hustler, A., Pearson, J., Bastkowski, S., Moxon, S., Swarbreck, D., Greenman, C.D., and Southgate, J. (2017). Heterarchy of transcription factors driving basal and luminal cell phenotypes in human urothelium. Cell Death Differ. *24*, 809–818.
30. Yoshihara, K., Shahmoradgoli, M., Martínez, E., Vegesna, R., Kim, H., Torres-Garcia, W., Treviño, V., Shen, H., Laird, P.W., Levine, D.A., et al. (2013). Inferring tumour purity and stromal and immune cell admixture from expression data. Nat. Commun. *4*, 2612.
31. Nirmal, A.J., Regan, T., Shih, B.B., Hume, D.A., Sims, A.H., and Freeman, T.C. (2018). Immune Cell Gene Signatures for Profiling the Microenvironment of Solid Tumors. Cancer Immunol. Res. *6*, 1388–1400.
32. Charoentong, P., Finotello, F., Angelova, M., Mayer, C., Efremova, M., Rieder, D., Hackl, H., and Trajanoski, Z. (2017). Pan-cancer Immunogenomic Analyses Reveal Genotype-Immunophenotype Relationships and Predictors of Response to Checkpoint Blockade. Cell Rep. *18*, 248–262.
33. Alexandrov, L.B., Ju, Y.S., Haase, K., Van Loo, P., Martincorena, I., Nik-Zainal, S., Totoki, Y., Fujimoto, A., Nakagawa, H., Shibata, T., et al. (2016). Mutational signatures associated with tobacco smoking in human cancer. Science *354*, 618–622.
34. Alexandrov, L.B., Kim, J., Haradhvala, N.J., Huang, M.N., Tian Ng, A.W., Wu, Y., Boot, A., Covington, K.R., Gordenin, D.A., Bergstrom, E.N., et al.; PCAWG Mutational Signatures Working Group; PCAWG Consortium (2020). The repertoire of mutational signatures in human cancer. Nature *578*, 94–101.
35. Kim, J., Mouw, K.W., Polak, P., Braunstein, L.Z., Kamburov, A., Kwiatkowski, D.J., Rosenberg, J.E., Van Allen, E.M., D'Andrea, A., and Getz, G. (2016). Somatic ERCC2 mutations are associated with a distinct genomic signature in urothelial tumors. Nat. Genet. *48*, 600–606.
36. Taber, A., Christensen, E., Lamy, P., Nordentoft, I., Prip, F., Lindskrog, S.V., Birkenkamp-Demtröder, K., Okholm, T.L.H., Knudsen, M., Pedersen, J.S., et al. (2020). Molecular correlates of cisplatin-based chemotherapy response in muscle invasive bladder cancer by integrated multi-omics analysis. Nat. Commun. *11*, 4858.
37. Martincorena, I., Raine, K.M., Gerstung, M., Dawson, K.J., Haase, K., Van Loo, P., Davies, H., Stratton, M.R., and Campbell, P.J. (2017). Universal Patterns of Selection in Cancer and Somatic Tissues. Cell *171*, 1029–1041.e21.
38. Robertson, A.G., Kim, J., Al-Ahmadie, H., Bellmunt, J., Guo, G., Cherniack, A.D., Hinoue, T., Laird, P.W., Hoadley, K.A., Akbani, R., et al.; TCGA Research Network (2017). Comprehensive Molecular Characterization of Muscle-Invasive Bladder Cancer. Cell *171*, 540–556.e25.
39. Smith, E.R., Cayrou, C., Huang, R., Lane, W.S., Côté, J., and Lucchesi, J.C. (2005). A human protein complex homologous to the Drosophila

MSL complex is responsible for the majority of histone H4 acetylation at lysine 16. Mol. Cell. Biol. *25*, 9175–9188.

40. Dou, Y., Milne, T.A., Tackett, A.J., Smith, E.R., Fukuda, A., Wysocka, J., Allis, C.D., Chait, B.T., Hess, J.L., and Roeder, R.G. (2005). Physical association and coordinate function of the H3 K4 methyltransferase MLL1 and the H4 K16 acetyltransferase MOF. Cell *121*, 873–885.
41. Sarkis, A.S., Dalbagni, G., Cordon-Cardo, C., Zhang, Z.-F., Sheinfeld, J., Fair, W.R., Herr, H.W., and Reuter, V.E. (1993). Nuclear overexpression of p53 protein in transitional cell bladder carcinoma: a marker for disease progression. J. Natl. Cancer Inst. *85*, 53–59.
42. Van Allen, E.M., Mouw, K.W., Kim, P., Iyer, G., Wagle, N., Al-Ahmadie, H., Zhu, C., Ostrovnaya, I., Kryukov, G.V., O'Connor, K.W., et al. (2014). Somatic ERCC2 mutations correlate with cisplatin sensitivity in muscle-invasive urothelial carcinoma. Cancer Discov. *4*, 1140–1153.
43. Liu, D., Plimack, E.R., Hoffman-Censits, J., Garraway, L.A., Bellmunt, J., Van Allen, E., and Rosenberg, J.E. (2016). Clinical Validation of Chemotherapy Response Biomarker ERCC2 in Muscle-Invasive Urothelial Bladder Carcinoma. JAMA Oncol. *2*, 1094–1096.
44. Plimack, E.R., Dunbrack, R.L., Brennan, T.A., Andrake, M.D., Zhou, Y., Serebriiskii, I.G., Slifker, M., Alpaugh, K., Dulaimi, E., Palma, N., et al. (2015). Defects in DNA Repair Genes Predict Response to Neoadjuvant Cisplatin-based Chemotherapy in Muscle-invasive Bladder Cancer. Eur. Urol. *68*, 959–967.
45. Teo, M.Y., Bambury, R.M., Zabor, E.C., Jordan, E., Al-Ahmadie, H., Boyd, M.E., Bouvier, N., Mullane, S.A., Cha, E.K., Roper, N., et al. (2017). DNA Damage Response and Repair Gene Alterations Are Associated with Improved Survival in Patients with Platinum-Treated Advanced Urothelial Carcinoma. Clin. Cancer Res. *23*, 3610–3618.
46. Teo, M.Y., Seier, K., Ostrovnaya, I., Regazzi, A.M., Kania, B.E., Moran, M.M., Cipolla, C.K., Bluth, M.J., Chaim, J., Al-Ahmadie, H., et al. (2018). Alterations in DNA Damage Response and Repair Genes as Potential Marker of Clinical Benefit From PD-1/PD-L1 Blockade in Advanced Urothelial Cancers. J. Clin. Oncol. *36*, 1685–1694.
47. Groenendijk, F.H., de Jong, J., Fransen van de Putte, E.E., Michaut, M., Schlicker, A., Peters, D., Velds, A., Nieuwland, M., van den Heuvel, M.M., Kerkhoven, R.M., et al. (2016). ERBB2 Mutations Characterize a Subgroup of Muscle-invasive Bladder Cancers with Excellent Response to Neoadjuvant Chemotherapy. Eur. Urol. *69*, 384–388.
48. Hahn, N.M., Necchi, A., Loriot, Y., Powles, T., Plimack, E.R., Sonpavde, G., Roupret, M., and Kamat, A.M. (2018). Role of Checkpoint Inhibition in Localized Bladder Cancer. Eur. Urol. Oncol. *1*, 190–198.
49. Li, Q., Damish, A.W., Frazier, Z., Liu, D., Reznichenko, E., Kamburov, A., Bell, A., Zhao, H., Jordan, E.J., Gao, S.P., et al. (2019). *ERCC2* Helicase Domain Mutations Confer Nucleotide Excision Repair Deficiency and Drive Cisplatin Sensitivity in Muscle-Invasive Bladder Cancer. Clin. Cancer Res. *25*, 977–988.
50. Milewska, M., Cremona, M., Morgan, C., O'Shea, J., Carr, A., Vellanki, S.H., Hopkins, A.M., Toomey, S., Madden, S.F., Hennessy, B.T., and Eustace, A.J. (2018). Development of a personalized therapeutic strategy for ERBB-gene-mutated cancers. Ther. Adv. Med. Oncol. *10*, 1758834017746040.
51. Wood, R.D., Mitchell, M., and Lindahl, T. (2005). Human DNA repair genes, 2005. Mutat. Res. *577*, 275–283.
52. Rosenberg, J.E., Hoffman-Censits, J., Powles, T., van der Heijden, M.S., Balar, A.V., Necchi, A., Dawson, N., O'Donnell, P.H., Balmanoukian, A., Loriot, Y., et al. (2016). Atezolizumab in patients with locally advanced and metastatic urothelial carcinoma who have progressed following treatment with platinum-based chemotherapy: a single-arm, multicentre, phase 2 trial. Lancet *387*, 1909–1920.
53. Ayers, M., Lunceford, J., Nebozhyn, M., Murphy, E., Loboda, A., Kaufman, D.R., Albright, A., Cheng, J.D., Kang, S.P., Shankaran, V., et al. (2017). IFN-γ-related mRNA profile predicts clinical response to PD-1 blockade. J. Clin. Invest. *127*, 2930–2940.
54. Biton, A., Bernard-Pierrot, I., Lou, Y., Krucker, C., Chapeaublanc, E., Rubio-Pérez, C., López-Bigas, N., Kamoun, A., Neuzillet, Y., Gestraud, P., et al. (2014). Independent component analysis uncovers the landscape of the bladder tumor transcriptome and reveals insights into luminal and basal subtypes. Cell Rep. *9*, 1235–1245.
55. Varley, C.L., Stahlschmidt, J., Lee, W.C., Holder, J., Diggle, C., Selby, P.J., Trejdosiewicz, L.K., and Southgate, J. (2004). Role of PPARgamma and EGFR signalling in the urothelial terminal differentiation programme. J. Cell Sci. *117*, 2029–2036.
56. Rochel, N., Krucker, C., Coutos-Thévenot, L., Osz, J., Zhang, R., Guyon, E., Zita, W., Vanthong, S., Hernandez, O.A., Bourguet, M., et al. (2019). Recurrent activating mutations of PPARγ associated with luminal bladder tumors. Nat. Commun. *10*, 253.
57. Korpal, M., Puyang, X., Jeremy Wu, Z., Seiler, R., Furman, C., Oo, H.Z., Seiler, M., Irwin, S., Subramanian, V., Julie Joshi, J., et al. (2017). Evasion of immunosurveillance by genomic alterations of PPARγ/RXRα in bladder cancer. Nat. Commun. *8*, 103.
58. Bernardo, C., Eriksson, P., Marzouka, N.A., Liedberg, F., Sjödahl, G., and Höglund, M. (2019). Molecular pathology of the luminal class of urothelial tumors. J. Pathol. *249*, 308–318.
59. Meeks, J.J., Carneiro, B.A., Pai, S.G., Oberlin, D.T., Rademaker, A., Fedorchak, K., Balasubramanian, S., Elvin, J., Beaubier, N., and Giles, F.J. (2016). Genomic characterization of high-risk non-muscle invasive bladder cancer. Oncotarget *7*, 75176–75184.
60. Bellmunt, J., Kim, J., Reardon, B., Perera-Bel, J., Orsola, A., Rodriguez-Vida, A., Wankowicz, S.A., Bowden, M., Barletta, J.A., Morote, J., et al. (2020). Genomic Predictors of Good Outcome, Recurrence, or Progression in High-Grade T1 Non-Muscle-Invasive Bladder Cancer. Cancer Res. *80*, 4476–4486.
61. Rasheed, S.A.K., Leong, H.S., Lakshmanan, M., Raju, A., Dadlani, D., Chong, F.T., Shannon, N.B., Rajarethinam, R., Skanthakumar, T., Tan, E.Y., et al. (2018). GNA13 expression promotes drug resistance and tumor-initiating phenotypes in squamous cell cancers. Oncogene *37*, 1340–1353.
62. Siehler, S. (2009). Regulation of RhoGEF proteins by G12/13-coupled receptors. Br. J. Pharmacol. *158*, 41–49.
63. Yagi, H., Asanoma, K., Ohgami, T., Ichinoe, A., Sonoda, K., and Kato, K. (2016). GEP oncogene promotes cell proliferation through YAP activation in ovarian cancer. Oncogene *35*, 4471–4480.
64. Zhang, Z., Tan, X., Luo, J., Cui, B., Lei, S., Si, Z., Shen, L., and Yao, H. (2018). GNA13 promotes tumor growth and angiogenesis by upregulating CXC chemokines via the NF-κB signaling pathway in colorectal cancer cells. Cancer Med. *7*, 5611–5620.
65. Maziarz, M., Park, J.C., Leyme, A., Marivin, A., Garcia-Lopez, A., Patel, P.P., and Garcia-Marcos, M. (2020). Revealing the Activity of Trimeric G-proteins in Live Cells with a Versatile Biosensor Design. Cell *182*, 770–785.e16.
66. Lawson, A.R.J., Abascal, F., Coorens, T.H.H., Hooks, Y., O'Neill, L., Latimer, C., Raine, K., Sanders, M.A., Warren, A.Y., Mahbubani, K.T.A., et al. (2020). Extensive heterogeneity in somatic mutation and selection in the human bladder. Science *370*, 75–82.
67. Li, C.G., Mahon, C., Sweeney, N.M., Verschueren, E., Kantamani, V., Li, D., Hennigs, J.K., Marciano, D.P., Diebold, I., Abu-Halawa, O., et al. (2019). PPARγ Interaction with UBR5/ATMIN Promotes DNA Repair to Maintain Endothelial Homeostasis. Cell Rep. *26*, 1333–1343.e7.
68. Khandekar, M.J., Banks, A.S., Laznik-Bogoslavski, D., White, J.P., Choi, J.H., Kazak, L., Lo, J.C., Cohen, P., Wong, K.K., Kamenecka, T.M., et al. (2018). Noncanonical agonist PPARγ ligands modulate the response to DNA damage and sensitize cancer cells to cytotoxic chemotherapy. Proc. Natl. Acad. Sci. USA *115*, 561–566.
69. De Simone, G., di Masi, A., Vita, G.M., Polticelli, F., Pesce, A., Nardini, M., Bolognesi, M., Ciaccio, C., Coletta, M., Turilli, E.S., et al. (2020).

Mycobacterial and Human Nitrobindins: Structure and Function. Antioxid. Redox Signal. *33*, 229–246.

70. Necchi, A., Raggi, D., Gallina, A., Ross, J.S., Farè, E., Giannatempo, P., Marandino, L., Colecchia, M., Lucianò, R., Bianchi, M., et al. (2020). Impact of Molecular Subtyping and Immune Infiltration on Pathological Response and Outcome Following Neoadjuvant Pembrolizumab in Muscle-invasive Bladder Cancer. Eur. Urol. *77*, 701–710.
71. Tamura, S., Wang, Y., Veeneman, B., Hovelson, D., Bankhead, A., 3rd, Broses, L.J., Lorenzatti Hiles, G., Liebert, M., Rubin, J.R., Day, K.C., et al. (2018). Molecular Correlates of *In Vitro* Responses to Dacomitinib and Afatinib in Bladder Cancer. Bladder Cancer *4*, 77–90.
72. Choudhury, N.J., Campanile, A., Antic, T., Yap, K.L., Fitzpatrick, C.A., Wade, J.L., 3rd, Karrison, T., Stadler, W.M., Nakamura, Y., and O'Donnell, P.H. (2016). Afatinib Activity in Platinum-Refractory Metastatic Urothelial Carcinoma in Patients With ERBB Alterations. J. Clin. Oncol. *34*, 2165–2171.
73. Cambier, S., Sylvester, R.J., Collette, L., Gontero, P., Brausi, M.A., van Andel, G., Kirkels, W.J., Silva, F.C., Oosterlinck, W., Prescott, S., et al. (2016). EORTC Nomograms and Risk Groups for Predicting Recurrence, Progression, and Disease-specific and Overall Survival in Non-Muscle-invasive Stage Ta-T1 Urothelial Bladder Cancer Patients Treated with 1-3 Years of Maintenance Bacillus Calmette-Guérin. Eur. Urol. *69*, 60–69.
74. Fernandez-Gomez, J., Solsona, E., Unda, M., Martinez-Piñeiro, L., Gonzalez, M., Hernandez, R., Madero, R., Ojea, A., Pertusa, C., Rodriguez-Molina, J., et al.; Club Urológico Español de Tratamiento Oncológico (CUETO) (2008). Prognostic factors in patients with non-muscle-invasive bladder cancer treated with bacillus Calmette-Guérin: multivariate analysis of data from four randomized CUETO trials. Eur. Urol. *53*, 992–1001.
75. Bastos, D.A., Mattedi, R.L., Barreiro, R., dos Santos, F.F., Buzatto, V., Masotti, C., Souza, J.M., de Lima, M.Z.T., Friguglietti, G.W., Dzik, C., et al. (2020). Genomic Biomarkers and Underlying Mechanism of Benefit from BCG Immunotherapy in Non-Muscle Invasive Bladder Cancer. Bladder Cancer *6*, 171–186.
76. Kates, M., Matoso, A., Choi, W., Baras, A.S., Daniels, M.J., Lombardo, K., Brant, A., Mikkilineni, N., McConkey, D.J., Kamat, A.M., et al. (2020). Adaptive Immune Resistance to Intravesical BCG in Non-Muscle Invasive Bladder Cancer: Implications for Prospective BCG-Unresponsive Trials. Clin. Cancer Res. *26*, 882–891.
77. Kamat, A.M., Dickstein, R.J., Messetti, F., Anderson, R., Pretzsch, S.M., Gonzalez, G.N., Katz, R.L., Khanna, A., Zaidi, T., Wu, X., et al. (2012). Use of fluorescence in situ hybridization to predict response to bacillus Calmette-Guérin therapy for bladder cancer: results of a prospective trial. J. Urol. *187*, 862–867.
78. Subramanian, A., Tamayo, P., Mootha, V.K., Mukherjee, S., Ebert, B.L., Gillette, M.A., Paulovich, A., Pomeroy, S.L., Golub, T.R., Lander, E.S., and Mesirov, J.P. (2005). Gene set enrichment analysis: a knowledge-based approach for interpreting genome-wide expression profiles. Proc. Natl. Acad. Sci. USA *102*, 15545–15550.
79. Gartner, J.J., Davis, S., Wei, X., Lin, J.C., Trivedi, N.S., Teer, J.K., Meltzer, P.S., Rosenberg, S.A., and Samuels, Y.; NISC Comparative Sequencing Program (2012). Comparative exome sequencing of metastatic lesions provides insights into the mutational progression of melanoma. BMC Genomics *13*, 505.
80. Blokzijl, F., Janssen, R., van Boxtel, R., and Cuppen, E. (2018). MutationalPatterns: comprehensive genome-wide analysis of mutational processes. Genome Med. *10*, 33.
81. Li, H., and Durbin, R. (2009). Fast and accurate short read alignment with Burrows-Wheeler transform. Bioinformatics *25*, 1754–1760.
82. Bergmann, E.A., Chen, B.J., Arora, K., Vacic, V., and Zody, M.C. (2016). Conpair: concordance and contamination estimator for matched tumor-normal pairs. Bioinformatics *32*, 3196–3198.
83. Li, H., Handsaker, B., Wysoker, A., Fennell, T., Ruan, J., Homer, N., Marth, G., Abecasis, G., and Durbin, R.; 1000 Genome Project Data Processing Subgroup (2009). The Sequence Alignment/Map format and SAMtools. Bioinformatics *25*, 2078–2079.
84. Benjamin, D., Sato, T., Cibulskis, K., Getz, G., Stewart, C., and Lichtenstein, L. (2019). Calling Somatic SNVs and Indels with Mutect2. bioRxiv. https://doi.org/10.1101/861054.
85. Fan, Y., Xi, L., Hughes, D.S., Zhang, J., Zhang, J., Futreal, P.A., Wheeler, D.A., and Wang, W. (2016). MuSE: accounting for tumor heterogeneity using a sample-specific error model improves sensitivity and specificity in mutation calling from sequencing data. Genome Biol. *17*, 178.
86. Koboldt, D.C., Zhang, Q., Larson, D.E., Shen, D., McLellan, M.D., Lin, L., Miller, C.A., Mardis, E.R., Ding, L., and Wilson, R.K. (2012). VarScan 2: somatic mutation and copy number alteration discovery in cancer by exome sequencing. Genome Res. *22*, 568–576.
87. Kim, S., Scheffler, K., Halpern, A.L., Bekritsky, M.A., Noh, E., Källberg, M., Chen, X., Kim, Y., Beyter, D., Krusche, P., and Saunders, C.T. (2018). Strelka2: fast and accurate calling of germline and somatic variants. Nat. Methods *15*, 591–594.
88. Shiraishi, Y., Sato, Y., Chiba, K., Okuno, Y., Nagata, Y., Yoshida, K., Shiba, N., Hayashi, Y., Kume, H., Homma, Y., et al. (2013). An empirical Bayesian framework for somatic mutation detection from cancer genome sequencing data. Nucleic Acids Res. *41*, e89.
89. Dunkler, D., Ploner, M., Schemper, M., and Heinze, G. (2018). Weighted Cox Regression Using the R Package coxphw. J. Stat. Softw. *84*.
90. Eble, J.N., Sauter, G., Epstein, J.I., and Sesterhenn, I.A. (2004). World Health Organization Classification of Tumours. Pathology and Genetics of Tumours of the Urinary System and Male Genital Organs (IARC Press Lyon).
91. Mostofi, F.K., Davis, C.J., Jr., Sesterhenn, I.A., and Sobin, L.H. (1973). Histological typing of urinary bladder tumours (Springer).
92. Mills, R.E., Luttig, C.T., Larkins, C.E., Beauchamp, A., Tsui, C., Pittard, W.S., and Devine, S.E. (2006). An initial map of insertion and deletion (INDEL) variation in the human genome. Genome Res. *16*, 1182–1190.
93. Marzouka, N.A., and Eriksson, P. (2021). multiclassPairs: An R package to train multiclass pairbased classifier. Bioinformatics, btab088.
94. Lambert, S.A., Jolma, A., Campitelli, L.F., Das, P.K., Yin, Y., Albu, M., Chen, X., Taipale, J., Hughes, T.R., and Weirauch, M.T. (2018). The Human Transcription Factors. Cell *172*, 650–665.
95. Fletcher, M.N., Castro, M.A., Wang, X., de Santiago, I., O'Reilly, M., Chin, S.F., Rueda, O.M., Caldas, C., Ponder, B.A., Markowetz, F., and Meyer, K.B. (2013). Master regulators of FGFR2 signalling and breast cancer risk. Nat. Commun. *4*, 2464.
96. Margolin, A.A., Wang, K., Lim, W.K., Kustagi, M., Nemenman, I., and Califano, A. (2006). Reverse engineering cellular networks. Nat. Protoc. *1*, 662–671.
97. R Core Team (2012). A language and environment for statistical computing (R Foundation for Statistical Computing).
98. Benjamini, Y., and Hochberg, Y. (1995). Controlling the false discovery rate: a practical and powerful approach to multiple testing. J. R. Stat. Soc. B *57*, 289–300.
99. Grambsch, P., and Therneau, T. (1994). Proportional hazards tests and diagnostics based on weighted residuals. Biometrika *81*, 515–526.
100. Schemper, M., Wakounig, S., and Heinze, G. (2009). The estimation of average hazard ratios by weighted Cox regression. Stat. Med. *28*, 2473–2489.

STAR★METHODS

KEY RESOURCES TABLE

REAGENT or RESOURCE	SOURCE	IDENTIFIER
Biological samples		
Fresh frozen tissue samples	Leeds Multidisciplinary Research Tissue Bank	N/A
Venous blood samples from bladder cancer patients	Leeds Multidisciplinary Research Tissue Bank	N/A
Critical Commercial Assays		
Affymetrix GeneChip Human Transcriptome Array 2.0 and Genechip WT PLUS Reagent Kit	Affymetrix	Cat# 902310
GeneChip Hybridization, Wash, and Stain Kit	Affymetrix	Cat# 900720
Gentra Puregene Tissue Kit	QIAGEN	Cat# 158667
HiSeq 3000	Illumina	N/A
NEBNext DNA Library Prep Master Mix Set for Illumina	New England BioLabs	Cat# E6040L
NEBNext Singleplex Oligos for Illumina	New England BioLabs	Cat# E7350L
NEBNext High-Fidelity 2X PCR Master Mix	New England BioLabs	Cat# M0541L
QIAamp DNA Mini Kit	QIAGEN	Cat# 51306
RNeasy Plus Micro Kit	QIAGEN	Cat# 74034
SureSelect^{XT} Human All Exon v6 Kit	Agilent Technologies, Inc	Cat# 5190-8864
Deposited Data		
Raw and processed Affymetrix microarray data	This study	GSE:163209
Whole exome sequence data	This study	EGAS00001005765
Targeted sequence data	This study	EGAS00001005766, EGAS00001005767
Software and algorithms		
Affymetrix Expression Console software	Affymetrix	https://www.thermofisher.com/us/en/home/life-science/microarray-analysis.html
GenePattern	Broad Institute	https://cloud.genepattern.org
GSEA	Subramanian et al.[78]	https://www.gsea-msigdb.org/gsea/
Nexus Copy Number	Biodiscovery, Inc	http://www.biodiscovery.com/nexus-copy-number
ngCGH	Gartner et al.[79]	https://github.com/seandavi/ngCGH
R version 3.6.1	The R Foundation for Statistical Computing	https://www.r-project.org/
R studio for Mac	R-Studio	https://www.rstudio.com/products/rstudio/download/
R2	Jan Koster, Academic Medical Center, Netherlands	R2: Genomics Analysis and visualization Platform; https://hgserver1.amc.nl:443/
dNdScv	Martincorena et al., 2017[37]	https://github.com/im3sanger/dndscv
MutationalPatterns	Blokzijl et al., 2018[80]	https://bioconductor.org/packages/release/bioc/html/MutationalPatterns.html

(*Continued on next page*)

Continued

REAGENT or RESOURCE	SOURCE	IDENTIFIER
ESTIMATE	Yoshihara et al.[30]	https://bioinformatics.mdanderson.org/public-software/estimate/
COSMIC mutational signatures v3	N/A	https://cancer.sanger.ac.uk/signatures/
FASTQC	The Babraham Bioinformatics group	https://www.bioinformatics.babraham.ac.uk/projects/fastqc/
Cutadapt	Marcel Martin 2011	https://github.com/marcelm/cutadapt/
BWA	Li et al.[81]	https://github.com/lh3/bwa
Picard	Broad Institute	https://broadinstitute.github.io/picard/
GATK3	Broad Institute	https://accounts.google.com/ServiceLogin?service=cloudconsole&passive=1209600&osid=1&continue=https://console.cloud.google.com/storage/browser/_details/gatk-software/package-archive/gatk/GenomeAnalysisTK-3.8-1-0-gf15c1c3ef.tar.bz2&followup=https://console.cloud.google.com/storage/browser/_details/gatk-software/package-archive/gatk/GenomeAnalysisTK-3.8-1-0-gf15c1c3ef.tar.bz2
ContEst	Broad Institute	http://software.broadinstitute.org/cancer/cga/contest
Conpair	Bergmann et al.[82]	https://github.com/nygenome/Conpair
samtools	Li et al., 2009[83]	http://samtools.sourceforge.net/
MuTect2	Benjamin et al.[84]	https://accounts.google.com/ServiceLogin?service=cloudconsole&passive=1209600&osid=1&continue=https://console.cloud.google.com/storage/browser/_details/gatk-software/package-archive/gatk/GenomeAnalysisTK-3.8-1-0-gf15c1c3ef.tar.bz2&followup=https://console.cloud.google.com/storage/browser/_details/gatk-software/package-archive/gatk/GenomeAnalysisTK-3.8-1-0-gf15c1c3ef.tar.bz2
MuSE	Fan et al.[85]	https://bioinformatics.mdanderson.org/public-software/muse/
VarScan 2	Koboldt et al.[86]	http://massgenomics.org/varscan
Strelka2	Kim et al.[87]	https://github.com/Illumina/strelka
EBCall	Shiraishi et al.[88]	https://github.com/friend1ws/EBCall
MeerKat	CBMI, Harvard Medical School	http://compbio.med.harvard.edu/Meerkat/
coxph	Therneau (2021). A Package for Survival Analysis in R. R package version 3.2-13.	https://cran.r-project.org/web/packages/survival/index.html
coxphw	Dunkler et al.[89]	N/A
RTN	Castro et al.[25]	http://www.bioconductor.org/packages/release/bioc/html/RTN.html

RESOURCE AVAILABILITY

Lead contact

Further information and requests for resources and reagents should be directed to and will be fulfilled by the lead contact, Margaret A. Knowles (m.a.knowles@leeds.ac.uk).

Materials Availability

This study did not generate new unique reagents.

Data and code availability

- Microarray data are available at the Gene Expression Omnibus under accession number GSE163209. Raw sequencing data are available at The European Genome-phenome Archive (EGA) under accession numbers EGAS00001005765, EGAS00001005766 and EGAS00001005767.
- This paper does not report original code.
- Any additional information required to reanalyze the data reported in this paper is available from the lead contact upon request.

EXPERIMENTAL MODEL AND SUBJECT DETAILS

Human Tissue Samples and Subject Follow-up Data

Clinical samples and associated clinical data were sourced from the Leeds Multidisciplinary Research Tissue Bank (REC reference: 20/YH/0103). All patients provided written informed consent for the use of their samples for medical research. Cold cup biopsies were collected, snap-frozen and stored in liquid nitrogen. The remainder of the sample was embedded in paraffin for diagnostic assessment. Samples were graded and staged by a consultant urological pathologist (J-A.R) using the 1973 and 2004 WHO and TNM criteria, respectively.[90,91] To avoid the risk of under-staging of T1 samples, all samples were re-evaluated by a single urological histopathologist (J-A.R) and when inadequate tissue was present in the surgical specimen, we only included those that were definitively re-evaluated as T1 at re-resection or at cystectomy. Available clinical information including gender and age were collected. Median follow-up time was 55 months (range 3-186 months). This and details of analysis platforms for each sample are given in Table S1A.

METHOD DETAILS

DNA Extraction

Genomic DNA was isolated from frozen tissue sections comprising at least 70% tumor cells using a QIAamp DNA Mini Kit or a Gentra PureGene Tissue Kit. DNA was extracted from venous blood samples using a Nucleon BACC DNA Extraction Kit or by salt precipitation.

Copy Number Analysis

Low pass whole genome sequencing or array-CGH were used to assess copy number alterations in all tumors. Next-generation sequencing libraries were constructed using NEBNext® reagents according to the manufacturer's instructions. Raw sequencing data was processed as described for whole exome sequencing (below). After BAM file generation, ngCGH was used to compare number of read counts between tumor and matched blood samples using a window size of 1000 reads.[79] GC correction and copy number calling using the FASST2 Segmentation Algorithm, a Hidden Markov Model (HMM) based approach, were carried out within the Nexus Copy Number software package. The significance threshold for segmentation was set at 1.0E-5 also requiring a minimum of 3 probes per segment and a maximum probe spacing of 1000 between adjacent probes before breaking a segment. The log ratio thresholds for single copy gain and single copy loss were set at either $\pm$ 0.15 or $\pm$ 0.2, respectively, with the cut-off employed being determined by examination of individual sample profiles. The log ratio thresholds for two or more copy gain and homozygous loss were set at 1 and -1 respectively. Array-CGH and copy number calling was carried out as described previously.[10] To facilitate the combined analysis of copy number data from NGS and array-based platforms, after CN calling all analysis was restricted to those genomic regions associated with BAC clones present on the 1Mb resolution CGH array. To conduct cluster analysis, each individual region associated with a BAC array clone was assigned a copy number class (0 = no copy number alteration; 1 = gain; 2 = high-level amplification; -1 = loss; -2 = high-level loss). One-way unsupervised hierarchical cluster analysis was conducted using Euclidean distance and the Ward method of linkage. For samples analyzed by CGH, fraction of genome altered (FGA) was defined as the percentage of clones reporting significantly altered copy number (gain or loss). For sample analyzed by NGS, FGA was calculated by dividing the sum of the lengths of all regions exhibiting altered copy number by the total length of the genome (hg38). FGA groups were defined as A (< 1%), B (1- < 10%), C (10- < 30%) and D (>30%). Copy number data for the 113 Ta samples and 18 of the 104 T1 samples were reported previously.[10,13]

RNA Extraction, Gene Expression Profiling and NMF analysis

Total RNA was isolated from frozen tissue sections using a RNeasy Plus Micro Kit and amplified using the Affymetrix GeneChip® WT PLUS Reagent Kit according to manufacturer's instructions. The resulting cDNA was quantified using OD (NanoDrop). The cDNA was normalized and hybridized onto Affymetrix Human Transcriptome 2.0 microarrays for 16 hours at 45°C. Microarrays were washed and stained using the Affymetrix GeneChip® Hybridization, Wash, and Stain Kit according to manufacturer's instructions using the Affymetrix GeneChip® Fluidics Station 450. Microarrays were scanned using an Affymetrix GeneChip® 7G microarray scanner. Quality control checks were conducted using Affymetrix® Expression Console Software (RRID:SCR_018718). Affymetrix HTA 2.0 CEL files were normalized as rma_sketch using apt-probeset-summarize from the Affymetrix Power Tools and HTA-2_0.r1.gene.cdf. After normalization, the dataset was loaded into the R2: genomics analysis and visualization platform (http://r2.amc.nl). R2 was used for routine data visualization, data mining and analysis. For NMF analysis, a text file containing the gene-level normalized natural log values for all samples was exported from R2. This datafile was converted to .gct format and preprocessed using the PreprocessDataset module in GenePattern (RRID:SCR_003201) with default settings. The preprocessed datafile was then used as input for the GenePattern NMFConsensus module (v5) with default settings. NMF analysis in Ta samples generated 3 clusters in a single step. For T1 samples two initial NMF clusters were re-analyzed independently, generating four final subtypes.

Whole Exome Sequencing

Libraries were generated using 3 μg of DNA and enriched for exonic regions using the SureSelect Human All Exon V6 Kit (58 tumor:-blood pairs) according to the manufacturer's protocols. Sequencing was performed on an Illumina HiSeq 3000 in paired-end mode with 150 bp read length and eight samples (four tumor:blood pairs) per lane. Base calling and quality control was performed using Illumina's Real Time Analysis software version 1.6 with standard settings. Sequence files were QC checked using FastQC (v0.10.0) (RRID:SCR_014583) before and after preprocessing. Adaptor contamination and low-quality read ends (< 20) were trimmed using Cutadapt 1.14 (RRID:SCR_011841). Any read in which either pair had a length less than 19 was removed from subsequent analysis.

Alignment was performed using the BWA.1 bwa-mem algorithm[81] (RRID:SCR_010910) to the GRCh38 reference genome. To avoid tumor-normal bias, we merged the tumor and its paired normal alignment bam files and performed pre-genotyping processes together. Because we would apply multiple somatic mutation calling tools in addition to MuTect2, we performed local realignment around indels first despite this being an omittable step for MuTect2 pipeline. This step was conducted using the GATK v3.8 RealignerTargetCreator and IndelRealigner (RRID:SCR_001876) in Smith-Waterman mode with reference to 1000 Genomes phase 3 indel sites, and Mills and 1000G gold standard sites.[92] Next, we followed the best practice of somatic mutation calling recommended by GATK3 for pre-processing, which includes duplicate reads marking (Picard) and base quality recalibration (GATK3). The tumor-normal pair was then separated and ready for somatic mutation calling. Quality metrics including target coverage [Picard (RRID:SCR_006525) and Samtools[83] (RRID:SCR_002105)] and contamination [Contest (RRID:SCR_000595) and Conpair2][82] were evaluated prior to genotyping. In particular for MuTect2 mutation calling, we created the panel-of-normal (PON) based on all the in-house exome sequencing data processed under the same protocol and lab facility (N = 68).

We aimed to develop a tailored somatic mutation calling protocol for our sequencing data. From several tools previously reviewed,[82] we evaluated and selected 5 somatic mutation calling tools: MuTect2 (RRID:SCR_000559), MuSE, EBCall (RRID:SCR_006791), VarScan2 (RRID:SCR_006849), and Strelka2 (RRID:SCR_005109),[84–88]based on their performance on in-house exome sequencing data benchmarked by different amounts of input DNA (200 ng to 3 μg). We selected mutations called by at least two callers for the downstream analysis. Following this the number of mutations per sample was approximately equal to the median number of mutations generated by the 5 callers. For all callers, post-calling filtration was applied and only variants that passed the build-in filtration by each software were kept. Variant annotation was performed based on Ensembl VEP GRCh38 release 90. Data for 17 Ta samples reported previously[13] was re-analyzed using Mutect2. SNV counts were based on Mutect2 calls only.

Targeted Sequencing

Targeted sequencing data from an in-house design for 40 genes was taken from a previous study[13] for 18 Ta samples (Table S1A). All other targeted sequencing used a new design for 140 genes. Agilent's SureDesign tool was used to design a 1.133 Mb SureSelect custom capture for all coding exons of the 140 selected candidate genes (Table S2). The design included a 10 base pair extension to the 3¢ and 5¢ ends of each region. Libraries were generated using 1.2 μg of DNA and enriched for targeted exonic regions according to the manufacturer's protocols for 112 tumor:blood pairs. Forty eight samples (24 tumor:blood pairs) were run in a single lane on an Illumina HiSeq 3000 in paired-end mode with 150 bp read length. Raw data handling up to FASTQ file generation was as described above.

Tumor mutational burden

Tumor mutational burden (TMB) was calculated as the number of somatic non-synonymous mutations per Mb of targeted DNA.

Mutation Significance Analysis

Putative driver genes were identified from whole exome sequence data from T1 samples using dNdScv[37] (RRID:SCR_017093). The dNdScv R package is a suite of maximum-likelihood dN/dS methods designed to quantify selection in cancer and somatic evolution.

The package contains functions to quantify dN/dS ratios for missense, nonsense and essential splice site mutations. The background mutation rate of each gene was estimated by combining local information (synonymous mutations in the gene) and global information (variation of the mutation rate across genes, exploiting epigenomic covariates), and controlling for the sequence composition of the gene and mutational signatures. dNdScv uses trinucleotide context-dependent substitution matrices to avoid common mutation biases affecting dN/dS. A pre-computed database for GRCh38 was downloaded for this analysis (https://github.com/im3sanger/dndscv_data/tree/master/data).

Analysis of Mutational Signatures

We used non-negative matrix factorization in the package MutationalPatterns[80] to derive signatures and to compare to COSMIC Mutational Signatures (https://cancer.sanger.ac.uk/signatures/) (RRID:SCR_002260) in both whole exome and target capture sequence data.

Gene expression signatures

We used gene lists associated with cell cycle, urothelial differentiation and its regulation (KLF5, PPARG, RXRA, ELF3, FOXA1, GATA3, TP63, GRHL2, GRHL3), FGFR3-related gene expression and DNA repair genes[9,18,54,51], and expression signatures described for PPARG signaling,[54] bladder CIS,[17] progression of NMIBC,[7,20] immune infiltration[19,31,32] and response to immune checkpoint inhibition.[52,53] Signature zscores for these genesets were derived for each sample, weighted where up- and downregulated genes were included. For estimation of immune infiltration we also used ESTIMATE.[30] Two epithelial signatures were a compiled list of cytokeratin genes (KRT8, KRT18, KRT19, KRT17, KRT5, KRT6, KRT13, KRT7, KRT20), EPCAM and CDH1, and a list of low-variance epithelial-expressed genes correlated with E-cadherin and EPCAM in urothelial tumor datasets (SPINT2, TACSTD2, EPCAM, KRT19, RAB25, GPR56, SDC1, SPINT1, CDH1, DDR1, CDS1, RAB5B, LAD1, PRPRF).

Classification of samples using UROMOL2021 and LundTax classifiers

Samples were classified according to the UROMOL2021 classes.[5] A Pearson correlation was computed between each sample's gene expression profile and each of the four centroids (the mean gene expression profile for each class) corresponding to the four NMIBC classes. Samples were then assigned to the class with the highest sample-centroid correlation. The UROMOL2021 NMIBC classifier is available as a web application at http://www.nmibc-class.dk.

The R package multiclassPairs[93] was used to generate a single sample version of the Lund classification system (LundTax).[21] Tumors were classified according to LundTax into Urothelial-like (Uro), Genomically Unstable (GU), Basal/Squamous-like (Ba/Sq), Mesenchymal-like (Mes-like), and small cell/neuroendocrine like (Sc/Ne-like) using gene expression data. Uro samples were classified to Uro subclasses, UroA, UroB, and UroC.

Regulon analysis

To identify regulators of molecular subtypes identified, we analyzed regulatory networks (regulons) for a comprehensive set of 1547 transcription factors[94] using *RTN*.[25-27] Gene level normalization (using SST-RMA) and signal summarization was conducted using Affymetrix® Expression Console Software. We inferred the regulons using the R package *RTN* (version 2.13.2), which is described elsewhere.[25,95] Briefly, gene expression matrices for a set of samples were used to estimate the associations between a transcription factor and all of its potential targets. We used Mutual Information (MI) to identify potential regulator-target associations, and Spearman's correlation to assign the direction of an inferred association. Associations with MI below a minimum threshold were eliminated by permutation analysis (BH-adjusted p value $< 1x10^{-5}$), and unstable interactions were removed by bootstrapping, to create a regulatory network. Regulons were additionally processed by the ARACNe algorithm to enrich the regulons with direct TF-target interactions.[96] We estimated regulon activity by a two-tailed gene set enrichment analysis (GSEA-2T), which is described elsewhere.[25,27] The GSEA-2T was performed in R[97] using the RTN package.[25] We fitted a Cox proportional hazards regression to further assess regulon activity and survival, using the *RTNsurvival* package.[27] For the Kaplan-Meier curve, we stratified the cohort into 2 groups – positive and negative dES – and evaluated differences between the groups for 200-month PFS and RFS, using a Log-rank test. This package reports BH-adjusted P values[98].

QUANTIFICATION AND STATISTICAL ANALYSIS

Statistical analysis of transcriptome data was done in R2. The statistical test LIMMA with FDR 0.01 was applied to identify genes differentially expressed between copy number and expression subtypes. FDR adjusted p values (q values) are given in Tables S3 and S8. Other statistical tests Fisher's exact, chi square, Mann-Whitney, Kruskal-Wallis tests and correlation analyses, survival curve generation using the Kaplan-Meier method and curve comparison using the Log-rank (Mantel-Cox) test were carried out using GraphPad Prism 8.2 for Mac. Comparison between groups used the Mann-Whitney or Kruskal-Wallis tests for continuous variables and Fisher's exact test and Chi square test for categorical variables. A post hoc Dunn's test was used for multiple comparison correction following Kruskal-Wallis analyses. Bonferroni adjustment of chi square p values was used. A significance level of 0.05 was used in all tests.

We used the 'cox.zph' R function (Therneau, 2021; R package version 3.2-13, 2021; https://cran.r-project.org/web/packages/survival/index.html) to assess the proportional hazards assumption of a Cox Regression analysis, assessing the association between the 'group' covariate and the outcomes RFS and PFS, and displayed the Schoenfeld residuals. The Schoenfeld plot gives an estimate of the time-dependent coefficient beta. If the proportional hazards assumption holds then the beta function is a horizontal line.[99] Systematic departures from the horizontal line indicate non-proportional hazards. This was not observed in the RFS and PFS Schoenfeld plots and the 'cox.zph' test was not statistically significant. However, we saw that survival curves crossed over for both RFS and PFS data at early time points, which suggested the presence of non-proportional hazards. As the testing power for the corresponding regression parameter can be reduced in the presence of non-proportional hazards,[89] we carried out Cox regression analysis to estimate long-term survival rate under both proportional and non-proportional hazards assumptions. The Cox regression model under proportional hazards assumption was carried out using the 'coxph' function from the *survival* R package (Therneau, 2021; R package version 3.2-13, 2021. https://cran.r-project.org/web/packages/survival/index.html) and under non-proportional assumption was carried out using the 'coxphw' function from the *coxphw* R Package.[89,100]

Gene Ontology, KEGG Pathway and Gene Set Enrichment Analysis

Significantly upregulated genes (LIMMA test, false discovery rate p value = 0.01) in each subtype comparison was used as input for Gene Ontology (GO) biological process analysis in R2. A cut off of nominal p value < 0.05 was implemented. Gene Set Enrichment Analysis v3.0[78] (RRID:SCR_003199) was carried out using all genes; genomic and expression subtypes were assigned as phenotypes and permuted 1000 times, the test dataset was collapsed to gene symbols and run against gene sets in the Hallmarks database (v7.1).

Cell Reports Medicine, Volume *2*

Supplemental information

Stage-stratified molecular profiling of non-muscle-invasive bladder cancer enhances biological, clinical, and therapeutic insight

Carolyn D. Hurst, Guo Cheng, Fiona M. Platt, Mauro A.A. Castro, Nour-al-dain S. Marzouka, Pontus Eriksson, Emma V.I. Black, Olivia Alder, Andrew R.J. Lawson, Sia V. Lindskrog, Julie E. Burns, Sunjay Jain, Jo-An Roulson, Joanne C. Brown, Jan Koster, A. Gordon Robertson, Inigo Martincorena, Lars Dyrskjøt, Mattias Höglund, and Margaret A. Knowles

Table S2. Genes selected for targeted sequencing. Related to Figures 1-3.

ACAN	EGFR	LARP1B	RAD21
AHNAK2	ELF3	LGALS8	RARG
AKT1	EP300	LPHN3	RB1
ARHGAP18	EPG5	LRRC7	RBM10
ARHGEF10	ERBB2	MAGI3	RBM6
ARHGEF3	ERBB3	MAML1	RHOA
ARID1A	ERCC2	MAPK8IP3	RHOB
ARID2	ESPL1	MECOM	RREB1
ARID4A	FANCA	MYCBP2	RXRA
ASH1L	FAT1	MYO5B	RYR2
ASXL2	FAT2	NAT10	SCN1A
ATM	FAT3	NCOR1	SLC25A48
ATP6V1B2	FAT4	NCSTN	SPTAN1
ATP7B	FBXW7	NF1	STAG1
B3GNT9	FGFR3	NFE2L2	STAG2
BRAF	FMN1	NFE2L3	STK38
BRCA2	FOXA1	NOTCH1	SYNE1
BTG2	FOXQ1	NOTCH2	SYNE2
C1ORF173	FREM2	NOTCH3	TET3
CACNA1D	HAUS6	NRAS	TEX15
CCND1	HEPACAM	OSMR	TNC
CCND3	HERC1	PAIP1	TP53
CDKN1A	HMCN1	PALM3	TRAK1
CDKN2A	HRAS	PCDHA9	TSC1
CDKN2B	HRNR	PDZD2	TSC2
CEP290	INADL	PGS1	TXNIP
CHD6	ITK	PHF3	UEVLD
CLTC	KDM3A	PIK3CA	USP47
CLU	KDM6A	PIK3R1	UTY
COL11A1	KIF16B	PIK3R4	VCAN
CPAMD8	KLF5	POLE	WHSC1L1
CREBBP	KMT2A	POLE2	WNK1
DLG4	KMT2C	POTEF	ZFHX3
DOPEY1	KMT2D	PTEN	ZFP36L1
DUX4L4	KRAS	RAB11FIP1	ZFYVE26

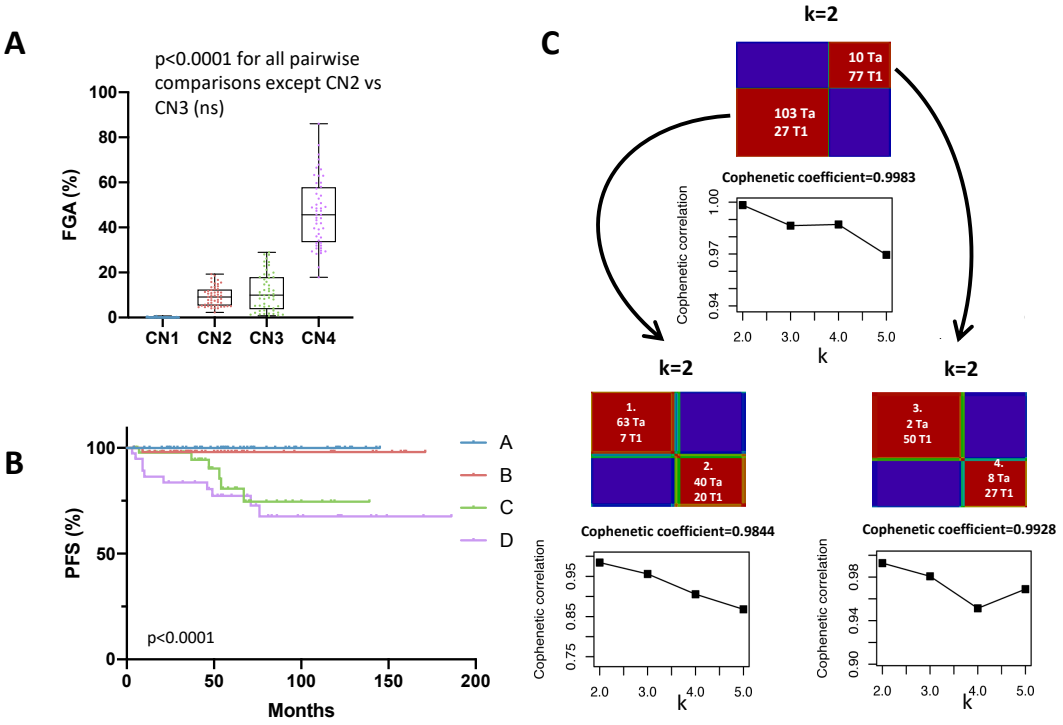
A
p<0.0001 for all pairwise comparisons except CN2 vs CN3 (ns)
FGA (%)
CN1
CN2
CN3
CN4
B
PFS (%)
p<0.0001
Months
A
B
C
D
C
k=2
10 Ta 77 T1
103 Ta 27 T1
Cophenetic coefficient=0.9983
Cophenetic correlation
k
k=2
1. 63 Ta 7 T1
2. 40 Ta 20 T1
Cophenetic coefficient=0.9844
k=2
3. 2 Ta 50 T1
4. 8 Ta 27 T1
Cophenetic coefficient=0.9928

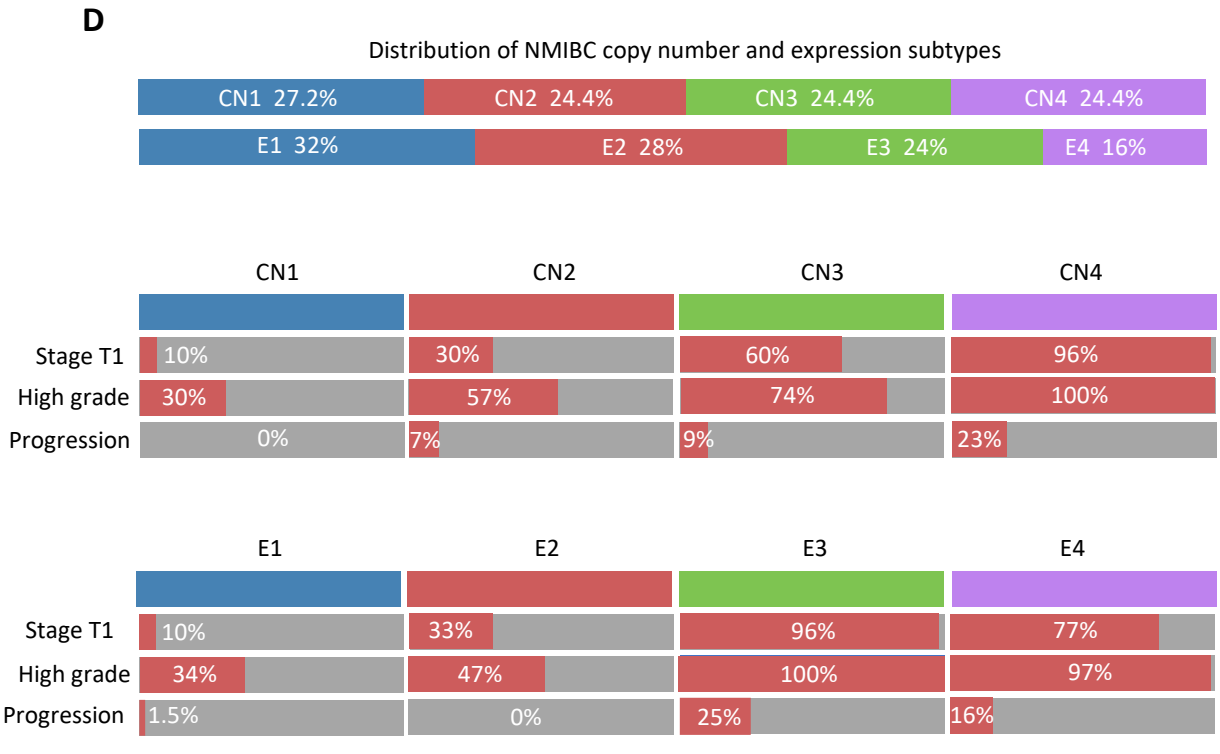
D
Distribution of NMIBC copy number and expression subtypes
CN1 27.2%
CN2 24.4%
CN3 24.4%
CN4 24.4%
E1 32%
E2 28%
E3 24%
E4 16%
CN1
CN2
CN3
CN4
Stage T1
10%
30%
60%
96%
High grade
30%
57%
74%
100%
Progression
0%
7%
9%
23%
E1
E2
E3
E4
Stage T1
10%
33%
96%
77%
High grade
34%
47%
100%
97%
Progression
1.5%
0%
25%
16%

Supplementary Figure 1. Features of copy number and expression subtypes of all 217 NMIBC. Related to Figure 1.

(A) Fraction of genome altered (FGA) in copy number subtypes CN1-CN4. Analysis of copy number data from NGS and array-based platforms was restricted to those genomic regions associated with BAC clones present on the 1Mb resolution CGH array. Each region was assigned a copy number class (0 = no copy number alteration; 1 = gain; 2 = high-level amplification; -1 = loss; -2 = high-level loss). FGA is defined as the percentage of clones reporting significantly altered copy number (gain or loss).

(B) Kaplan-Meier plots of progression-free survival (PFS) of NMIBC patients according to Fraction of Genome Altered (FGA) with tumors assigned to arbitrary groups with <1% FGA (A), 1-<10% FGA (B), 10-<30% FGA (C) and ≥30% FGA (D).

(C) Derivation of four NMIBC expression subtypes by two stage NMF analysis, showing subdivision of tumors of stage Ta and T1 into clusters and plots of cophenetic coefficients among k clusters for each analysis.

(D) Top, distribution of copy number and expression subtypes in 217 NMIBC. Lower panels show tumor stage, grade and progression frequencies according to subtypes.

(A) Kruskal-Wallis test with Dunn's multiple comparison correction. Mean, 25th and 75^{th} percentiles, minimum and maximum values are shown. **(B)** Log-rank analysis.

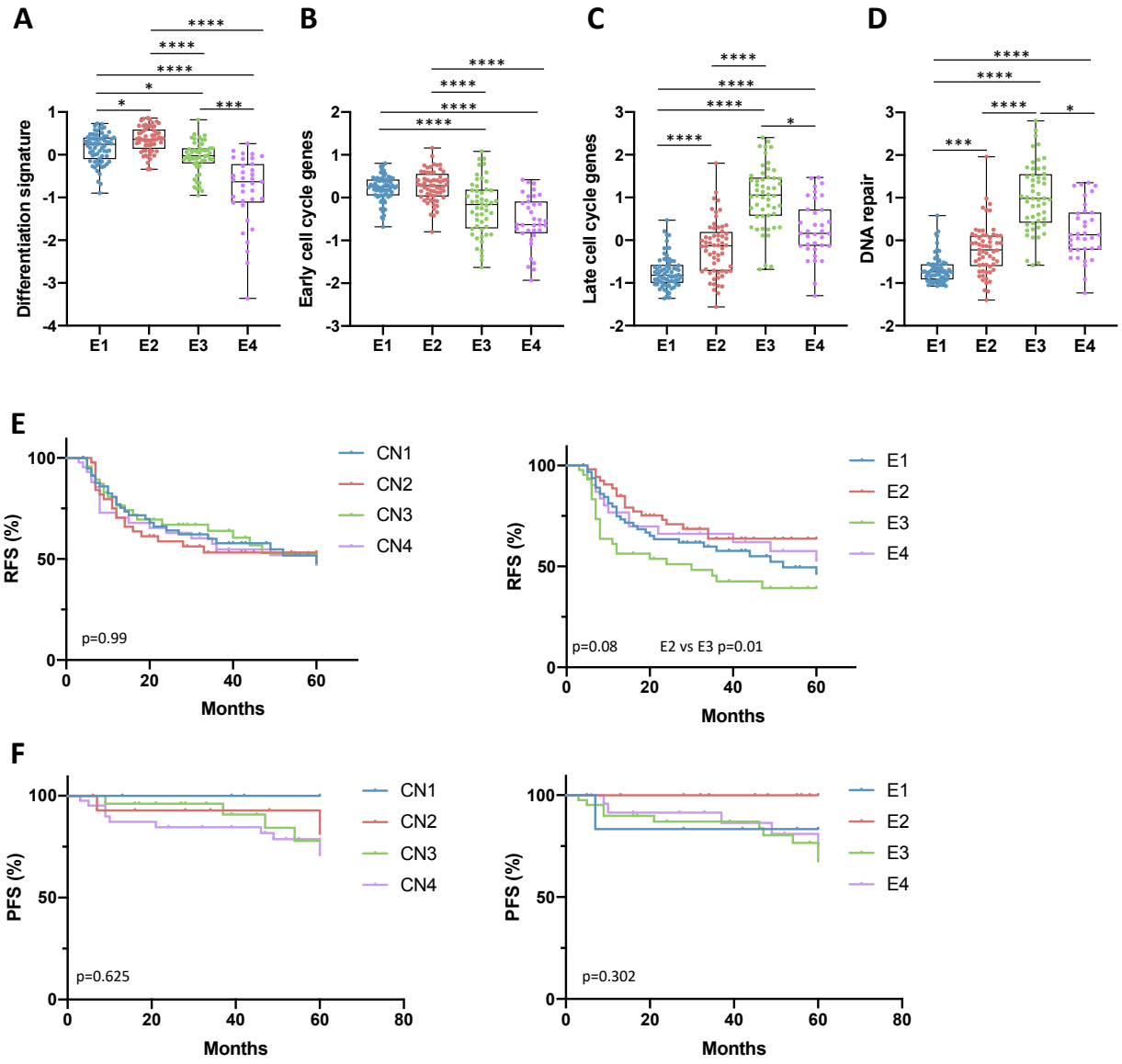
A
B
C
D
Differentiation signature
Early cell cycle genes
Late cell cycle genes
DNA repair
E1
E2
E3
E4
E
RFS (%)
CN1
CN2
CN3
CN4
p=0.99
Months
p=0.08
E2 vs E3 p=0.01
F
PFS (%)
p=0.625
p=0.302

Supplementary Figure 2. Expression signatures, recurrence-free survival and progression-free survival of NMIBC subtypes. Related to Figure 1.

(A) Urothelial differentiation signature in NMIBC expression subtypes.

(B) Expression of early cell cycle genes in NMIBC expression subtypes.

(C) Expression of late cell cycle genes in NMIBC expression subtypes.

(D) Expression of DNA repair genes in NMIBC expression subtypes.

(E) Kaplan-Meier plots of recurrence-free survival (RFS) according to NMIBC copy number subtypes CN1-CN4 (left) and expression subtypes E1-E4 (right).

(F) Kaplan-Meier plots of PFS of patients with T1 tumors only according to NMIBC copy number (left) and expression subtypes (right).

(A-D) Group measurements compared using Kruskal-Wallis test with Dunn's multiple comparison correction. Mean, 25th and 75^{th} percentiles, minimum and maximum values are shown. Adjusted p values; ****$p<0.0001$, ***$p<0.001$, **$p<0.01$, *$p<0.05$. **(E** and **F)** Log-rank analysis.

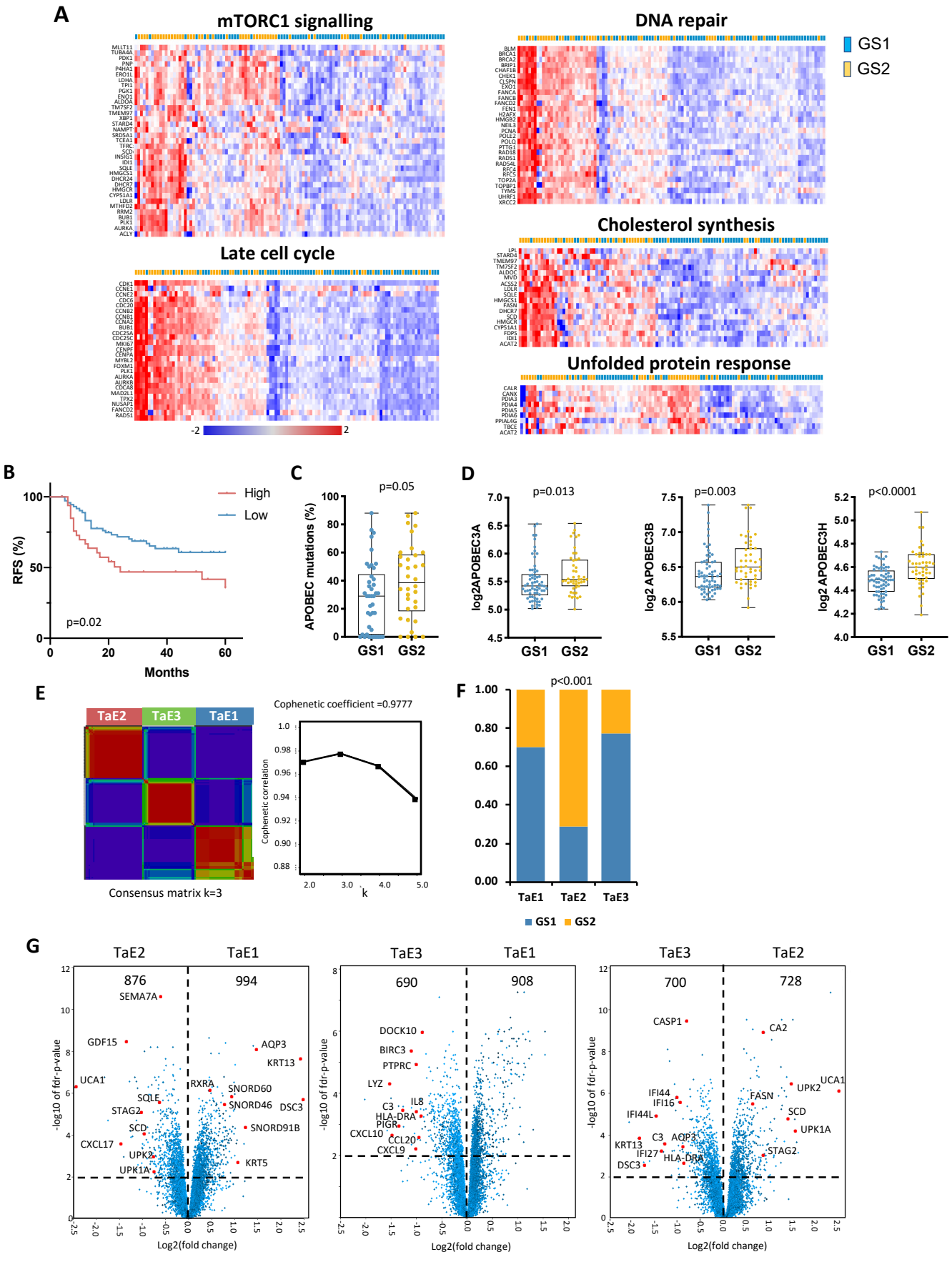
A
mTORC1 signalling
DNA repair
Late cell cycle
Cholesterol synthesis
Unfolded protein response
GS1
GS2
-2
2
B
High
Low
RFS (%)
p=0.02
Months
C
p=0.05
APOBEC mutations (%)
GS1
GS2
D
p=0.013
log2APOBEC3A
p=0.003
log2 APOBEC3B
p<0.0001
log2 APOBEC3H
E
TaE2
TaE3
TaE1
Consensus matrix k=3
Cophenetic coefficient =0.9777
Cophenetic correlation
k
F
p<0.001
TaE1
TaE2
TaE3
GS1
GS2
G
TaE2
TaE1
876
994
SEMA7A
GDF15
UCA1
SQLE
STAG2
SCD
CXCL17
UPK2
UPK1A
AQP3
KRT13
RXRA
SNORD60
SNORD46
DSC3
SNORD91B
KRT5
-log10 of fdr-p-value
Log2(fold change)
TaE3
TaE1
690
908
DOCK10
BIRC3
PTPRC
LYZ
C3
IL8
HLA-DRA
PIGR
CXCL10
CCL20
CXCL9
TaE3
TaE2
700
728
CASP1
CA2
UCA1
UPK2
IFI44
IFI16
FASN
IFI44L
SCD
UPK1A
KRT13
C3
AQP3
IFI27
HLA-DRA
STAG2
DSC3

Supplementary Figure 3. Features of stage Ta tumors according to Ta-derived genomic and expression subtypes. Related to Figure 2.

(A) Heatmaps of z-scores derived by clustering of expression levels of differentially expressed gene categories in genomic subtypes GS1 and GS2. Top bar in each panel indicates GS1 and GS2 assignment.

(B) Recurrence-free survival (RFS) according to high and low tumor grade. Log-rank analysis.

(C) Percentage of APOBEC-related mutations according to Ta tumor genomic subtype.

(D) mRNA expression levels of APOBEC3A, 3B and 3H in Ta genomic subtype tumors.

(E) Left, plot of NMF consensus clusters for three Ta expression subtypes TaE1-TaE3. Right, plot showing cophenetic coefficients among k clusters.

(F) Relationships of Ta genomic and expression subtypes.

(G) Volcano plots of genes differentially expressed (LIMMA test) between Ta tumor expression subtypes TaE1-TaE3 with false discovery rate $p<0.01$. Numbers of significantly up-regulated genes in each comparison are indicated at the top of each plot. Selected genes are indicated.

(B) Log-rank analysis. **(C** and **D)** Mann-Whitney test. Mean, 25th and 75^{th} percentiles, minimum and maximum values are shown. **(F)** Chi-square test with Bonferroni correction.

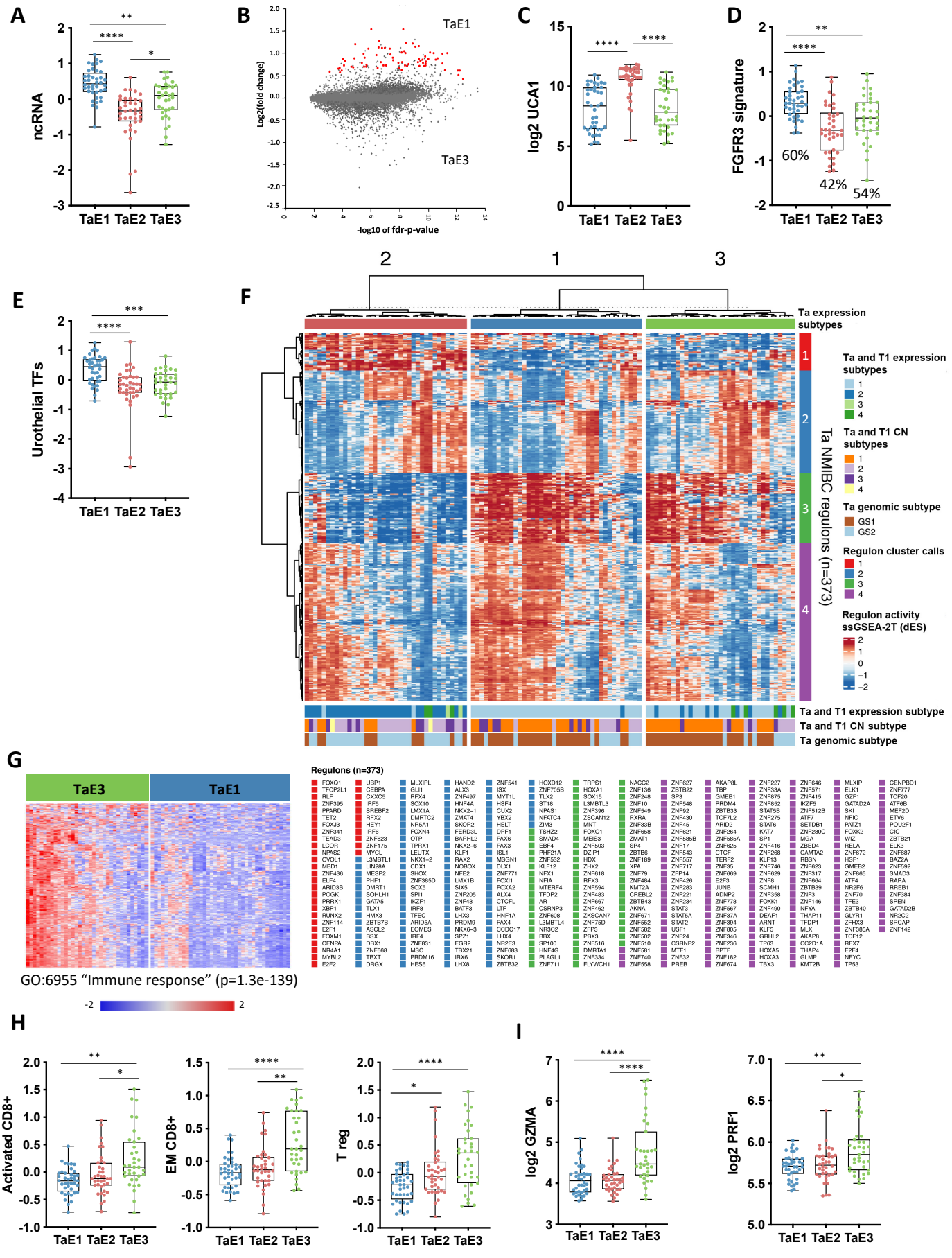
A
ncRNA
TaE1 TaE2 TaE3
B
TaE1
TaE3
Log2(fold change)
-log10 of fdr-p-value
C
log2 UCA1
TaE1 TaE2 TaE3
D
FGFR3 signature
60%
42%
54%
TaE1 TaE2 TaE3
E
Urothelial TFs
TaE1 TaE2 TaE3
F
2
1
3
Ta expression subtypes
Ta NMIBC regulons (n=373)
Ta and T1 expression subtypes
Ta and T1 CN subtypes
Ta genomic subtype
Regulon cluster calls
Regulon activity ssGSEA-2T (dES)
Ta and T1 expression subtype
Ta and T1 CN subtype
Ta genomic subtype
G
TaE3
TaE1
Regulons (n=373)
GO:6955 “Immune response” (p=1.3e-139)
H
Activated CD8+
EM CD8+
T reg
TaE1 TaE2 TaE3
I
log2 GZMA
log2 PRF1
TaE1 TaE2 TaE3

Supplementary Figure 4. Expression differences between stage Ta tumor genomic and expression subtypes. Related to Figure 2.

(A) Non-coding RNA signature (GO:16070) according to Ta expression subtypes.

(B) MA plot of genes differentially expressed between TaE1 and T1E3. Small nucleolar RNAs with higher expression in T1E1 are marked in red.

(C) Expression of UCA1 in Ta expression subtypes.

(D) FGFR3-related signature according to Ta expression subtypes. *FGFR3* mutation frequencies are indicated.

(E) Scores for expression of transcription factors (TFs) implicated in urothelial differentiation.

(F) Heatmap of regulon activity for 373 regulons with differential activity in stage Ta tumors supervised by Ta expression subtype. Expression and genomic covariates are shown below.

(G) Heatmap of z-scores for genes in GO:6955 "Immune response" in Ta expression subtypes TaE1 and TaE3.

(H) Scores for selected immune signatures [S1] in Ta expression subtypes. Activated DC8+ (left); EM, effector memory (middle); T reg, T regulatory (right).

(I) Expression levels of granzyme (GZMA) (left) and perforin 1 (PRF1) (right) in Ta expression subtypes.

(A, C, D, E, H and **I)** Group measurements compared using Kruskal-Wallis test with Dunn's multiple comparison correction. Mean, 25th and 75th percentiles, minimum and maximum values are shown. Adjusted p values; ****p<0.0001, ***p<0.001, **p<0.01, *p<0.05.

Table S4. snoRNAs differentially expressed in comparisons of Ta expression subgroups. Related to Figure 2.

TaE1 vs 2		TaE1 vs 3	
SNORA11	SNORD119	SNORA11	SNORD15B
SNORA12	SNORD11B	SNORA12	SNORD18A
SNORA14A	SNORD12	SNORA14A	SNORD32B
SNORA20	SNORD126	SNORA20	SNORD35B
SNORA21	SNORD127	SNORA21	SNORD37
SNORA22	SNORD12B	SNORA22	SNORD41
SNORA23	SNORD13	SNORA23	SNORD42A
SNORA24	SNORD14E	SNORA24	SNORD46
SNORA26	SNORD15B	SNORA26	SNORD58A
SNORA30	SNORD18A	SNORA30	SNORD58C
SNORA37	SNORD32B	SNORA37	SNORD59B
SNORA47	SNORD35B	SNORA47	SNORD60
SNORA48	SNORD37	SNORA48	SNORD61
SNORA49	SNORD41	SNORA49	SNORD70
SNORA50	SNORD42A	SNORA50	SNORD71
SNORA52	SNORD46	SNORA52	SNORD78
SNORA54	SNORD58A	SNORA54	SNORD8
SNORA57	SNORD58C	SNORA57	SNORD82
SNORA5A	SNORD59B	SNORA5A	SNORD85
SNORA65	SNORD60	SNORA65	SNORD9
SNORA68	SNORD61	SNORA68	SNORD91B
SNORA71B	SNORD70	SNORA71B	SNORD92
SNORD10	SNORD71	SNORD10	SNORD94
SNORD104	SNORD78	SNORD104	SNORD97
SNORD105	SNORD8	SNORD105	SNORD99
SNORD105B	SNORD82	SNORD105B	SNORA28
SNORD11	SNORD85	SNORD11	SNORA71D
SNORD111	SNORD9	SNORD111	SNORA76
SNORD111B	SNORD91B	SNORD111B	SNORD12C
SNORD116-1	SNORD92	SNORD116-1	SNORD59A
SNORD116-11	SNORD94	SNORD116-11	SNORD63
SNORD116-12	SNORD97	SNORD116-12	SNORA10
SNORD116-14	SNORD99	SNORD116-14	SNORA14B
SNORD116-15	SNORA45	SNORD116-15	SNORA16B
SNORD116-16	SNORD113-5	SNORD116-16	SNORA38B
SNORD116-18	SNORD115-14	SNORD116-18	SNORA5C
SNORD116-2	SNORD53	SNORD116-2	SNORA70C
SNORD116-23	SNORD93	SNORD116-23	SNORA70D
SNORD116-24	SNORA28	SNORD116-24	SNORA70E
SNORD116-25	SNORA71D	SNORD116-25	SNORA71A
SNORD116-26	SNORA76	SNORD116-26	SNORA71C
SNORD116-27	SNORD12C	SNORD116-27	SNORA80B
SNORD116-29	SNORD59A	SNORD116-29	SNORD121A
SNORD116-8	SNORD63	SNORD116-8	SNORD123
SNORD117	SNORD90	SNORD117	SNORD14A
		SNORD119	SNORD15A
		SNORD11B	SNORD16
		SNORD12	SNORD3A
		SNORD126	SNORD3C
		SNORD127	SNORD69
		SNORD12B	SNORD83A
		SNORD13	SNORD91A
		SNORD14E	SNORD116-13

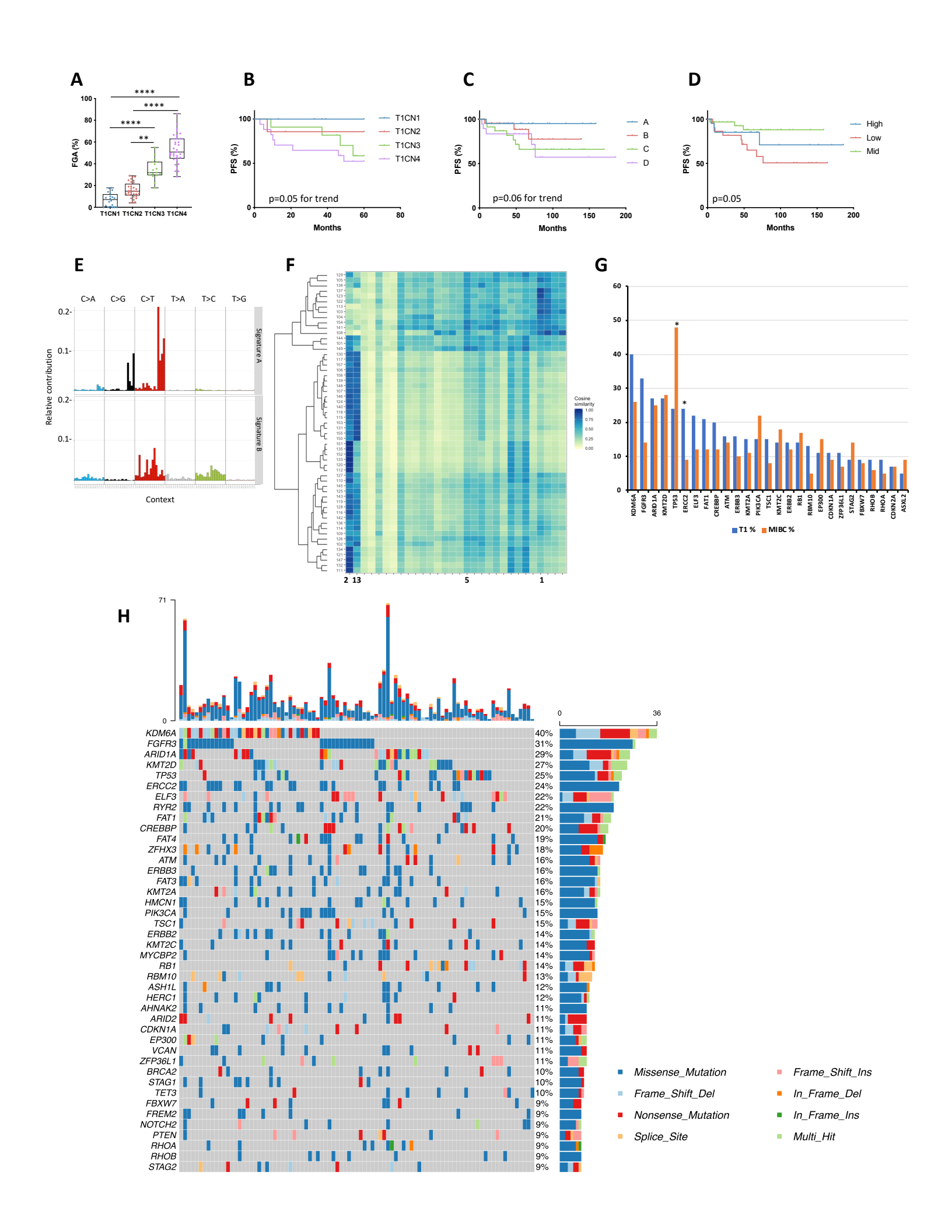
A
FGA (%)
T1CN1 T1CN2 T1CN3 T1CN4
B
PFS (%)
T1CN1
T1CN2
T1CN3
T1CN4
p=0.05 for trend
Months
C
PFS (%)
A
B
C
D
p=0.06 for trend
Months
D
PFS (%)
High
Low
Mid
p=0.05
Months
E
C>A C>G C>T T>A T>C T>G
Relative contribution
Signature A
Signature B
Context
F
Cosine similarity
G
T1 %
MIBC %
KDM6A FGFR3 ARID1A KMT2D TP53 ERCC2 ELF3 FAT1 CREBBP ATM ERBB3 KMT2A PIK3CA TSC1 KMT2C ERBB2 RB1 RBM10 EP300 CDKN1A ZFP36L1 STAG2 FBXW7 RHOB RHOA CDKN2A ASXL2
H
KDM6A 40%
FGFR3 31%
ARID1A 29%
KMT2D 27%
TP53 25%
ERCC2 24%
ELF3 22%
RYR2 22%
FAT1 21%
CREBBP 20%
FAT4 19%
ZFHX3 18%
ATM 16%
ERBB3 16%
FAT3 16%
KMT2A 16%
HMCN1 15%
PIK3CA 15%
TSC1 15%
ERBB2 14%
KMT2C 14%
MYCBP2 14%
RB1 14%
RBM10 13%
ASH1L 12%
HERC1 12%
AHNAK2 11%
ARID2 11%
CDKN1A 11%
EP300 11%
VCAN 11%
ZFP36L1 11%
BRCA2 10%
STAG1 10%
TET3 10%
FBXW7 9%
FREM2 9%
NOTCH2 9%
PTEN 9%
RHOA 9%
RHOB 9%
STAG2 9%
Missense_Mutation
Frame_Shift_Ins
Frame_Shift_Del
In_Frame_Del
Nonsense_Mutation
In_Frame_Ins
Splice_Site
Multi_Hit

Supplementary Figure 5. Genomic features of stage T1 tumors. Related to Figure 3.

(A) Fraction of Genome Altered (FGA%) according to T1 copy number subtypes T1CN1-T1CN4.

(B) Kaplan-Meier plots of PFS according to T1 copy number subtypes T1CN1-T1CN4.

(C) Kaplan-Meier plots of PFS according to Fraction of Genome Altered (FGA) of patients with T1 tumors assigned to arbitrary groups with <1% FGA (A), 1-<10% FGA (B), 10-<30% FGA (C) and ≥30% FGA (D).

(D) Kaplan-Meier plots of progression-free survival (PFS) according to tumor mutational burden. High, top 25%; Mid, middle 50%; Low, lowest 25%.

(E) Trinucleotide mutational profiles from two signatures extracted from whole exome data using NMF analysis in MutationalPatterns.

(F) Heatmap generated in MutationalPatterns showing identification of COSMIC mutational signatures in T1 tumors. Signatures 2 and 13 which are attributed to the activity of APOBEC cytidine deaminases, SBS1 and SBS5 are indicated.

(G) Comparison of the frequencies of mutations identified $\geq$ 5% of T1 tumors with those reported in muscle-invasive bladder tumors [S2].

(H) Oncoplot showing genes mutated in $\geq$ 9% of T1 tumors. Data for genes included in the 140 gene target capture. See Table S5 for prediction of oncogenic drivers from whole exome data.

(A) Kruskal-Wallis test with Dunn's multiple comparison correction. Mean, 25th and 75th percentiles, minimum and maximum values are shown. Adjusted p values; ****p<0.0001, **p<0.01. **(B-D)** Log-rank analysis. **(G)** Fisher's exact test with Bonferroni correction. Asterisks indicate p<0.01.

Table S6. dNdScv analysis of exome data from T1 tumors. Related to Figure 3.

Gene	Synonymous mutations	Missense mutations	Nonsense mutations	Essential splice site	Indels	dN/dS – missense*	dN/dS – nonsense*	dN/dS – indels*	q-value missense mutations	q-value truncating mutations	q-value (all genes)	q-value (known bladder cancer genes)	significance all genes	known bladder cancer genes
KDM6A	2	4	9	2	12	1.485510846	28.06428314	59.51189176	0.792690954	1.84E-06	2.17E-12	6.88E-15	TRUE	TRUE
TP53	0	13	4	0	4	20.25419979	58.93851075	71.99831236	3.16E-05	0.010714376	6.84E-11	2.17E-13	TRUE	TRUE
ELF3	1	4	2	0	9	5.371672988	26.28859173	171.5766234	0.783760701	0.897278091	1.82E-09	5.76E-12	TRUE	TRUE
ARID1A	2	8	11	1	6	1.970017649	30.86657391	18.61373692	0.783760701	2.87E-07	4.48E-09	1.42E-11	TRUE	TRUE
FGFR3	2	21	0	0	2	11.86845137	0	17.53234553	1.77E-05	0.897278091	4.73E-06	1.50E-08	TRUE	TRUE
RB1	0	0	3	1	5	0	19.58206803	38.16918067	0.783760701	0.384810895	0.000228603	7.25E-07	TRUE	TRUE
CDKN1A	0	2	1	0	4	6.352842167	28.29451632	171.9232429	0.783760701	0.897278091	0.00043603	1.38E-06	TRUE	TRUE
KMT2D	2	13	8	2	7	1.785312361	14.09890579	8.964036904	0.783760701	0.002188136	0.00043603	1.38E-06	TRUE	TRUE
ZFP36L1	1	5	1	0	4	7.453908566	30.21378992	83.67945449	0.783760701	0.897278091	0.00043603	1.38E-06	TRUE	TRUE
ARID2	1	4	10	0	0	1.411549215	24.34705699	0	0.817148289	4.00E-05	0.000820136	2.60E-06	TRUE	TRUE
FAM229A	0	3	0	0	3	11.49345738	0	166.2148539	0.783760701	0.897357875	0.003971316	NA	TRUE	FALSE
ERCC2	1	13	0	0	1	9.508835961	0	9.31909825	0.020714612	0.897278091	0.028903276	0.0001057	FALSE	TRUE
SPA17	0	2	0	0	3	7.424679135	0	139.9704033	0.783760701	0.897278091	0.028903276	NA	FALSE	FALSE
TSC1	5	7	3	2	3	1.955453408	13.71759019	18.26223288	0.783760701	0.263760412	0.028903276	0.0001057	FALSE	TRUE
PTEN	0	2	2	0	3	3.11728669	28.404692	52.66213194	0.783760701	0.897278091	0.028903276	0.0001057	FALSE	TRUE
CREBBP	0	12	5	0	3	4.380993841	16.70750866	8.708760255	0.783760701	0.263760412	0.033449633	0.000121161	FALSE	TRUE
EP300	8	13	3	0	7	1.58981765	2.760988549	20.55603991	0.783760701	0.897278091	0.264231139	0.0012841	FALSE	TRUE
ERBB3	1	12	0	0	1	5.501520469	0	5.280591041	0.783760701	0.897278091	0.999804434	0.007835389	FALSE	TRUE
PIK3CA	1	10	0	0	1	5.452910411	0	6.634082103	0.783760701	0.897278091	0.999804434	0.011517583	FALSE	TRUE
STAG2	1	2	1	1	3	0.861942431	6.510764538	16.76556446	0.940156287	0.897278091	0.999804434	0.016367923	FALSE	TRUE
FBXW7	2	7	3	0	0	4.564784934	16.05640084	0	0.783760701	0.897278091	0.999804434	0.016460315	FALSE	TRUE
ERBB2	5	13	0	1	1	3.896005194	3.101184214	5.646364465	0.783760701	0.897278091	0.999804434	0.021392185	FALSE	TRUE
RHOA	1	3	0	0	1	8.248049147	0	36.55584416	0.783760701	0.897278091	0.999804434	0.024896042	FALSE	TRUE
KANSL1	0	0	2	0	1	0	11.5226294	6.412146264	0.783760701	0.897278091	0.999804434	0.025531368	FALSE	TRUE
GNA13	2	5	0	0	1	5.485490625	0	18.76146499	0.783760701	0.897278091	0.999804434	0.028946739	FALSE	TRUE

* Maximum likelihood estimates obtained by dNdScv for missense mutations, nonsense mutations and indels.
Grey shading indicates results from restricted hypothesis testing of known bladder cancer genes (qrht < 0.05).
FAM229A excluded as somatic missense mutations create a rare germline SNP of unknown significance.
SPA17 excluded as all mutations in same sample.

Table S7. *ERBB2* and *ERBB3* mutations and *ERBB2* copy number in T1 tumors. Related to Figure 4.

Sample	*ERBB2* mutation	*ERBB3* mutation	*ERBB2* copy number status	*ERCC2* mutation status	Expression subtype	Copy number subtype
1081	NA	NA	Normal	NA	1	1
1106	p.S310F; p.C311Sfs*10	p.P590S	Normal	p.E606K; p.V604Rfs*103	1	1
1137	Wildtype	Wildtype	Normal	p.T484M	1	1
1315	NA	NA	Normal	NA	1	1
1408	Wildtype	Wildtype	Loss	p.E86Q	1	1
2020	Wildtype	Wildtype	Normal	Wildtype	1	1
2046	Wildtype	Wildtype	Normal	Wildtype	1	1
2390	Wildtype	Wildtype	Normal	p.N238S	1	1
589	NA	NA	Normal	NA	2	1
1062	p.A1243T; c.1737+2T>C	p.G284R	Normal	Wildtype	2	1
571	NA	NA	Normal	NA	3	1
1279	p.D636Pfs*8	Wildtype	Normal	p.N238S	3	1
1318	Wildtype	Wildtype	Normal	p.T76I	3	1
1747	Wildtype	Wildtype	Normal	p.V242F	3	1
1831	p.N259S	p.E150K	Normal	p.S381F; p.T484M	3	1
2165	Wildtype	Wildtype	Normal	Wildtype	3	1
2437	Wildtype	Wildtype	Normal	Wildtype	3	1
1729	Wildtype	Wildtype	Normal	Wildtype	4	1
1766	Wildtype	p.M433I	Normal	p.G665A	4	1
2138	Wildtype	Wildtype	Normal	Wildtype	4	1
94	Wildtype	Wildtype	Normal	Wildtype	1	2
315	NA	NA	Normal	NA	1	2
557	Wildtype	Wildtype	Amp/Gain	Wildtype	1	2
866	NA	NA	Normal	NA	1	2
1094	NA	NA	Normal	NA	1	2
1210	NA	NA	Amp/Gain	NA	1	2
1222	Wildtype	Wildtype	Normal	Wildtype	1	2
1481	Wildtype	Wildtype	Normal	Wildtype	1	2
1968	Wildtype	Wildtype	Normal	Wildtype	1	2
2103	p.S310F	Wildtype	Amp/Gain	Wildtype	1	2
2272	Wildtype	Wildtype	Normal	Wildtype	1	2
1358	Wildtype	p.R679Q	Amp/Gain	Wildtype	2	2
1428	Wildtype	Wildtype	Normal	p.N238S	2	2
1457	Wildtype	Wildtype	Normal	Wildtype	2	2
1629	Wildtype	Wildtype	Normal	Wildtype	2	2
1978	Wildtype	p.V104L	Normal	Wildtype	2	2
2056	Wildtype	Wildtype	Amp/Gain	Wildtype	2	2
2155	Wildtype	Wildtype	Amp/Gain	Wildtype	2	2
555	Wildtype	Wildtype	Normal	Wildtype	3	2
936	Wildtype	Wildtype	Normal	Wildtype	3	2
940	Wildtype	Wildtype	Normal	Wildtype	3	2
1395	Wildtype	Wildtype	Normal	Wildtype	3	2
1443	Wildtype	Wildtype	Amp/Gain	Wildtype	3	2
1521	Wildtype	Wildtype	Normal	Wildtype	3	2
1633	Wildtype	Wildtype	Normal	Wildtype	3	2
1679	Wildtype	Wildtype	Normal	Wildtype	3	2
1810	Wildtype	Wildtype	Normal	p.P463S	3	2
1933	Wildtype	Wildtype	Amp/Gain	Wildtype	3	2
2175	Wildtype	Wildtype	Normal	p.E86Q	3	2
377	Wildtype	Wildtype	Normal	Wildtype	4	2
418	Wildtype	Wildtype	Normal	Wildtype	4	2
534	Wildtype	Wildtype	Normal	Wildtype	4	2
1234	Wildtype	Wildtype	Amp/Gain	Wildtype	4	2
1817	p.R103Q	p.Q298E	Amp/Gain	p.Q662H	4	2
1087	Wildtype	Wildtype	Normal	Wildtype	1	3
1138	NA	NA	Normal	NA	1	3
1145	NA	NA	Normal	NA	1	3
1325	Wildtype	Wildtype	Normal	p.L633V	1	3
1392	Wildtype	Wildtype	Normal	Wildtype	1	3
2429	Wildtype	Wildtype	Normal	Wildtype	1	3
567	Wildtype	Wildtype	Normal	Wildtype	2	3
1023	Wildtype	Wildtype	Normal	Wildtype	2	3

1252	Wildtype	Wildtype	Amp/Gain	Wildtype	2	3
1300	p.E766Q; p.G778D	p.G582E	Normal	Wildtype	2	3
1407	Wildtype	Wildtype	Normal	Wildtype	2	3
1517	Wildtype	Wildtype	Normal	Wildtype	2	3
1735	Wildtype	Wildtype	Normal	Wildtype	2	3
2022	Wildtype	Wildtype	Amp/Gain	Wildtype	2	3
1860	p.V697L	Wildtype	Amp/Gain	p.N238S	3	3
2356	Wildtype	Wildtype	Normal	Wildtype	3	3
2224	p.R103Q	p.Q298E	Normal	p.T76I	4	3
393	Wildtype	Wildtype	Amp/Gain	Wildtype	2	4
544	Wildtype	Wildtype	Amp/Gain	Wildtype	2	4
1211	Wildtype	Wildtype	Loss	Wildtype	2	4
1934	Wildtype	Wildtype	Amp/Gain	Wildtype	2	4
2000	Wildtype	Wildtype	Loss	Wildtype	2	4
2033	p.L651V	Wildtype	Normal	Wildtype	2	4
2139	p.S250F; p.S609Y	Wildtype	Amp/Gain	p.N238S	2	4
2169	Wildtype	Wildtype	Normal	Wildtype	2	4
2178	Wildtype	Wildtype	Normal	Wildtype	2	4
2222	Wildtype	p.K747N	Normal	Wildtype	2	4
132	p.E238Q; p.S310F	p.I600M	Normal	Wildtype	3	4
435	p.E507K	p.M91I; p.E150*	Amp/Gain	p.S246F	3	4
1047	Wildtype	Wildtype	Amp/Gain	Wildtype	3	4
1124	Wildtype	Wildtype	Amp/Gain	Wildtype	3	4
1974	Wildtype	Wildtype	Normal	Wildtype	3	4
2058	Wildtype	Wildtype	Amp/Gain	Wildtype	3	4
411	NA	NA	Amp/Gain	NA	4	4
930	NA	NA	Amp/Gain	NA	4	4
1016	Wildtype	Wildtype	Amp/Gain	Wildtype	4	4
1249	Wildtype	Wildtype	Normal	Wildtype	4	4
1419	Wildtype	p.V104L	Normal	p.T484M	4	4
1503	Wildtype	Wildtype	Amp/Gain	Wildtype	4	4
1530	Wildtype	Wildtype	Normal	Wildtype	4	4
1559	Wildtype	Wildtype	Amp/Gain	Wildtype	4	4
1745	Wildtype	Wildtype	Amp/Gain	Wildtype	4	4
1853	p.D277H	Wildtype	Amp/Gain	Wildtype	4	4
1947	Wildtype	Wildtype	Amp/Gain	p.R658G	4	4
2037	Wildtype	Wildtype	Amp/Gain	Wildtype	4	4
2064	Wildtype	Wildtype	Amp/Gain	Wildtype	4	4
2214	Wildtype	p.L74F	Amp/Gain	p.Y24C	4	4
2223	Wildtype	p.D863N	Normal	p.E606Q	4	4
2267	Wildtype	Wildtype	Normal	p.N238S	4	4
2423	Wildtype	Wildtype	Amp/Gain	Wildtype	4	4

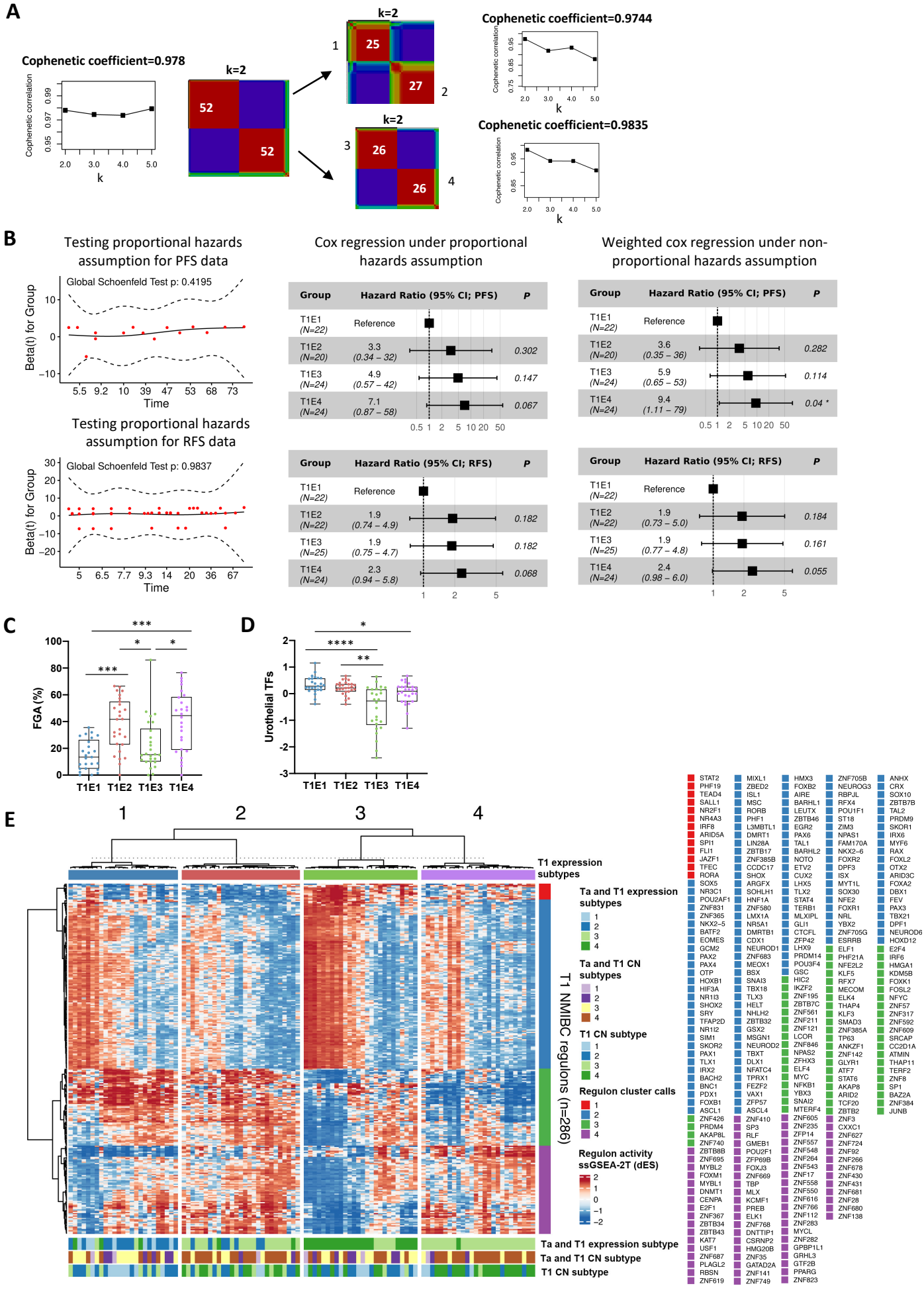
A
Cophenetic coefficient=0.978
Cophenetic correlation
k
k=2
52
52
1
25
27
2
3
26
26
4
Cophenetic coefficient=0.9744
Cophenetic coefficient=0.9835
B
Testing proportional hazards assumption for PFS data
Global Schoenfeld Test p: 0.4195
Beta(t) for Group
Time
Testing proportional hazards assumption for RFS data
Global Schoenfeld Test p: 0.9837
Cox regression under proportional hazards assumption
Weighted cox regression under non-proportional hazards assumption
Group
Hazard Ratio (95% CI; PFS)
P
T1E1 (N=22) Reference
T1E2 (N=20) 3.3 (0.34 – 32) 0.302
T1E3 (N=24) 4.9 (0.57 – 42) 0.147
T1E4 (N=24) 7.1 (0.87 – 58) 0.067
T1E1 (N=22) Reference
T1E2 (N=20) 3.6 (0.35 – 36) 0.282
T1E3 (N=24) 5.9 (0.65 – 53) 0.114
T1E4 (N=24) 9.4 (1.11 – 79) 0.04 *
Group
Hazard Ratio (95% CI; RFS)
P
T1E1 (N=22) Reference
T1E2 (N=22) 1.9 (0.74 – 4.9) 0.182
T1E3 (N=25) 1.9 (0.75 – 4.7) 0.182
T1E4 (N=24) 2.3 (0.94 – 5.8) 0.068
T1E1 (N=22) Reference
T1E2 (N=22) 1.9 (0.73 – 5.0) 0.184
T1E3 (N=25) 1.9 (0.77 – 4.8) 0.161
T1E4 (N=24) 2.4 (0.98 – 6.0) 0.055
C
FGA (%)
T1E1 T1E2 T1E3 T1E4
D
Urothelial TFs
T1E1 T1E2 T1E3 T1E4
E
1 2 3 4
T1 expression subtypes
Ta and T1 expression subtypes
Ta and T1 CN subtypes
T1 CN subtype
Regulon cluster calls
Regulon activity ssGSEA-2T (dES)
T1 NMIBC regulons (n=286)
Ta and T1 expression subtype
Ta and T1 CN subtype
T1 CN subtype

Supplementary Figure 6. Derivation and features of T1 tumor expression subtypes. Related to Figure 5.

(A) Derivation of four stage T1 expression subtypes by two stage NMF analysis, showing numbers of tumors in clusters and plots of cophenetic coefficients among k clusters for each analysis.

(B) Left, Schoenfeld plots for RFS and PFS data for T1 expression subtypes (see STAR Methods). Middle and right, forest plots showing results of Cox regression analyses under proportional and non-proportional hazards assumptions for RFS and PFS of T1 expression subtypes using the 'coxph' function (Therneau, 2021; R package version 3.2-13, 2021. https://CRAN.R-project.org/package=survival) and 'coxphw' [S3].

(C) Fraction of genome altered (FGA) according to T1 expression subtypes.

(D) Scores for expression of transcription factors (TFs) implicated in urothelial differentiation according to T1 expression subtypes.

(E) Heatmap of regulon activity for 286 regulons with differential activity in stage T1 tumors supervised by T1 expression subtype. Expression and genomic covariates are shown below.

(C and **D)** Kruskal-Wallis test with Dunn's multiple comparison correction. Mean, 25th and 75^{th} percentiles, minimum and maximum values are shown. Adjusted p values; ****p<0.0001, ***p<0.001, **p<0.01, *p<0.05.

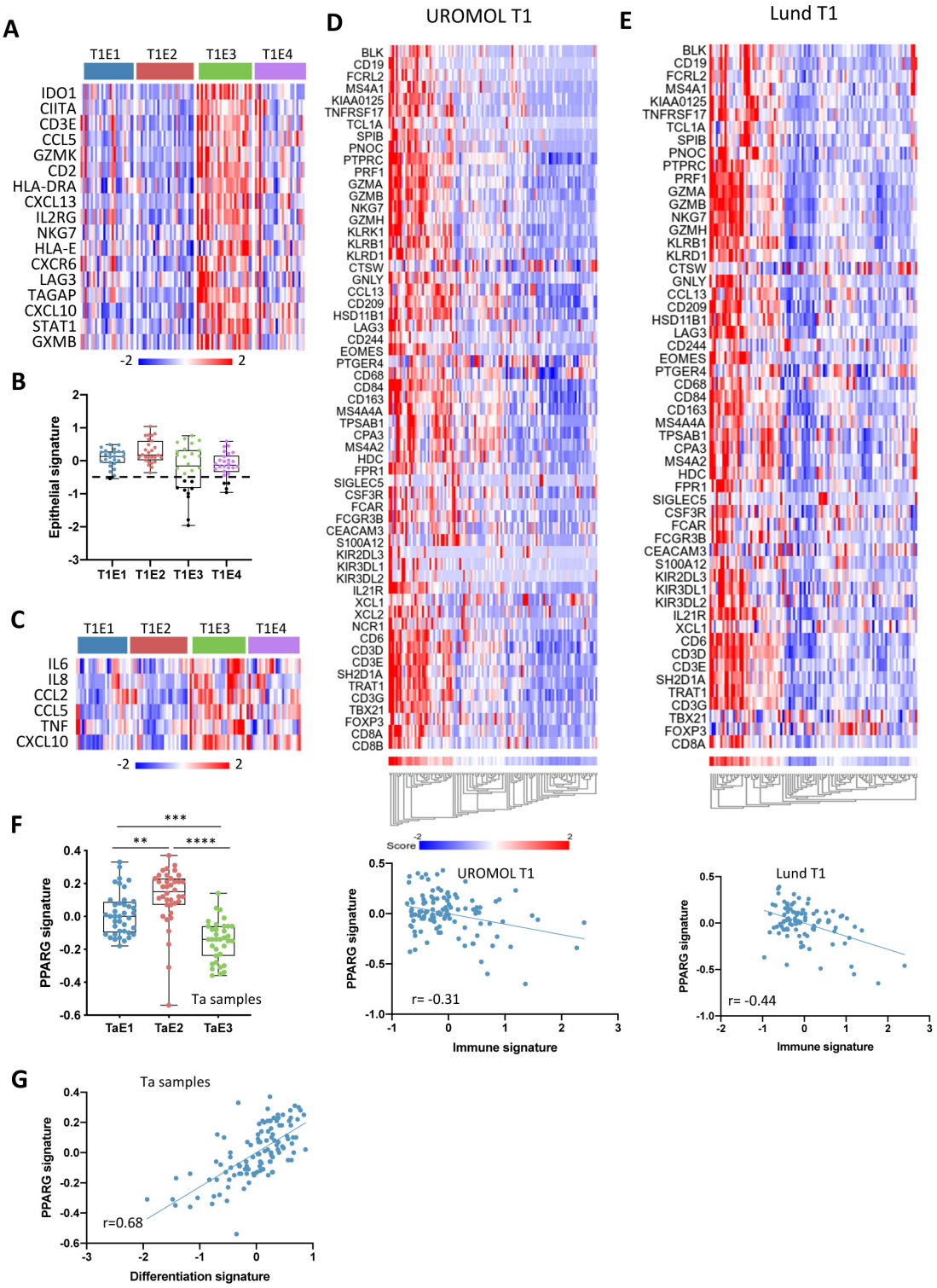
A
T1E1
T1E2
T1E3
T1E4
IDO1
CIITA
CD3E
CCL5
GZMK
CD2
HLA-DRA
CXCL13
IL2RG
NKG7
HLA-E
CXCR6
LAG3
TAGAP
CXCL10
STAT1
GXMB
-2
2
B
Epithelial signature
T1E1
T1E2
T1E3
T1E4
C
IL6
IL8
CCL2
CCL5
TNF
CXCL10
D
UROMOL T1
BLK
CD19
FCRL2
MS4A1
KIAA0125
TNFRSF17
TCL1A
SPIB
PNOC
PTPRC
PRF1
GZMA
GZMB
NKG7
GZMH
KLRK1
KLRB1
KLRD1
CTSW
GNLY
CCL13
CD209
HSD11B1
LAG3
CD244
EOMES
PTGER4
CD68
CD84
CD163
MS4A4A
TPSAB1
CPA3
MS4A2
HDC
FPR1
SIGLEC5
CSF3R
FCAR
FCGR3B
CEACAM3
S100A12
KIR2DL3
KIR3DL1
KIR3DL2
IL21R
XCL1
XCL2
NCR1
CD6
CD3D
CD3E
SH2D1A
TRAT1
CD3G
TBX21
FOXP3
CD8A
CD8B
Score
UROMOL T1
PPARG signature
r= -0.31
Immune signature
E
Lund T1
Lund T1
PPARG signature
r= -0.44
Immune signature
F
***
**
****
PPARG signature
Ta samples
TaE1
TaE2
TaE3
G
Ta samples
PPARG signature
r=0.68
Differentiation signature

Supplementary Figure 7. Relationship of PPARG signature to immune infiltration in NMIBC. Related to Figure 6.

(A) Heatmap of z-scores for genes in a T-cell inflamed signature [S4] in T1 expression subtypes.

(B) Expression scores for a panel of epithelial marker genes (see Methods) used to provide an estimate of epithelial tumor cell content in T1 samples. Samples with zscores < -0.05 indicated by black dots were removed from analysis of the relationship of PPARG signature and tumor infiltration. Mean, 25th and 75th percentiles, minimum and maximum values are shown.

(C) Heatmap of z-scores for pro-inflammatory chemokines that attract effector T cells that were shown to be regulated by PPARG in T24 bladder tumor cells [S5] in T1 expression subtypes.

(D) Heatmap of z-scores for 60-gene immune signature [S6] in T1 tumors reported in the first UROMOL study [S7] (ArrayExpress: E-MTAB-4321). Graph below shows correlation of PPARG and immune signatures scores.

(E) Heatmap of z-scores for 60-gene immune signature in T1 tumors from the study of Sjodahl *et al* [S8] (GSE: 32894). Graph below shows correlation of PPARG and immune signatures scores.

(F) PPARG signature score in Ta expression subtypes.

(G) Correlation of PPARG signature and urothelial differentiation signature in Ta samples.

(F) Kruskal-Wallis test test with Dunn's multiple comparison correction. Mean, 25th and 75th percentiles, minimum and maximum values are shown. Adjusted p values; ****p<0.0001, ***p<0.001, **p<0.01. **(D** and **E** lower panels and **G)** Pearson r.

Supplemental references

S1. Charoentong, P., Finotello, F., Angelova, M., Mayer, C., Efremova, M., Rieder, D., Hackl, H., and Trajanoski, Z. (2017). Pan-cancer Immunogenomic Analyses Reveal Genotype-Immunophenotype Relationships and Predictors of Response to Checkpoint Blockade. Cell Rep *18*, 248-262. 10.1016/j.celrep.2016.12.019.

S2. Robertson, A.G., Kim, J., Al-Ahmadie, H., Bellmunt, J., Guo, G., Cherniack, A.D., Hinoue, T., Laird, P.W., Hoadley, K.A., Akbani, R., et al. (2017). Comprehensive Molecular Characterization of Muscle-Invasive Bladder Cancer. Cell, 540-556. 10.1016/j.cell.2017.09.007.

S3. Dunkler, D., Ploner, M., Schemper, M., and Heinze, G. (2018). Weighted Cox Regression Using the R Package coxphw. J Statistical Software *84*. doi: 10.18637/jss.v084.i02.

S4. Ayers, M., Lunceford, J., Nebozhyn, M., Murphy, E., Loboda, A., Kaufman, D.R., Albright, A., Cheng, J.D., Kang, S.P., Shankaran, V., et al. (2017). IFN-gamma-related mRNA profile predicts clinical response to PD-1 blockade. J. Clin. Invest. *127*, 2930-2940. 10.1172/JCI91190.

S5. Korpal, M., Puyang, X., Jeremy Wu, Z., Seiler, R., Furman, C., Oo, H.Z., Seiler, M., Irwin, S., Subramanian, V., Julie Joshi, J., et al. (2017). Evasion of immunosurveillance by genomic alterations of PPARgamma/RXRalpha in bladder cancer. Nat Commun *8*, 103. 10.1038/s41467-017-00147-w.

S6. Danaher, P., Warren, S., Dennis, L., D'Amico, L., White, A., Disis, M.L., Geller, M.A., Odunsi, K., Beechem, J., and Fling, S.P. (2017). Gene expression markers of Tumor Infiltrating Leukocytes. Journal for immunotherapy of cancer *5*, 18. 10.1186/s40425-017-0215-8.

S7. Hedegaard, J., Lamy, P., Nordentoft, I., Algaba, F., Hoyer, S., Ulhoi, B.P., Vang, S., Reinert, T., Hermann, G.G., Mogensen, K., et al. (2016). Comprehensive Transcriptional Analysis of Early-Stage Urothelial Carcinoma. Cancer Cell *30*, 27-42. 10.1016/j.ccell.2016.05.004.

S8. Sjodahl, G., Lauss, M., Lovgren, K., Chebil, G., Gudjonsson, S., Veerla, S., Patschan, O., Aine, M., Ferno, M., Ringner, M., et al. (2012). A molecular taxonomy for urothelial carcinoma. Clin. Cancer Res. *18*, 3377-3386. 10.1158/1078-0432.CCR-12-0077-T.